NASA TECHNICAL NOTE

NASA TN D-4987

NASA TN D-4987

FLIGHT PERFORMANCE OF FW-4D SOLID-PROPELLANT ROCKET MOTOR ON DELTA 50 (AIMP-E)

by Daniel Dembrow

Goddard Space Flight Center
Greenbelt, Md.

NATIONAL AERONAUTICS AND SPACE ADMINISTRATION • WASHINGTON, D. C. • MARCH 1969

NASA TN D-4987

FLIGHT PERFORMANCE OF FW-4D SOLID-PROPELLANT ROCKET MOTOR ON DELTA 50 (AIMP-E)

By Daniel Dembrow

Goddard Space Flight Center
Greenbelt, Md.

NATIONAL AERONAUTICS AND SPACE ADMINISTRATION

For sale by the Clearinghouse for Federal Scientific and Technical Information
Springfield, Virginia 22151 – CFSTI price $3.00

ABSTRACT

This paper summarizes the in-flight performance of the FW-4D solid-propellant rocket motor used as the third stage of the Delta 50 launch vehicle for the first Anchored Interplanetary Monitoring Platform (AIMP-E), Lunar Explorer. This was the first Delta to use a digital integrating accelerometer for accurately determining third-stage velocity. The instrumentation included a rocket-chamber pressure transducer, a longitudinal accelerometer, and a counter and encoder for converting the digital accelerometer output into two forms: integrated acceleration × time (i.e., velocity) pulses and accumulated pulse count. Four IRIG subcarrier channels fed the performance data to a 3-watt FM/FM phase-modulated telemetry transmitter operating on a 256.2-MHz carrier. The correlation between predicted and observed third-stage performance was excellent. Incremental velocity, chamber pressure, and longitudinal acceleration were used to calculate propellant specific impulses. The high resolution velocity meter detected a slight continuous post-burnout velocity increase lasting about 50 seconds and caused presumably by third-stage motor outgassing.

CONTENTS

FLIGHT PERFORMANCE OF FW-4D SOLID-PROPELLANT ROCKET MOTOR ON DELTA 50 (AIMP-E)

by
Daniel Dembrow
Goddard Space Flight Center

INTRODUCTION

Delta 50, which launched the first Lunar Explorer, also called Anchored Interplanetary Monitoring Platform E (AIMP-E), on July 19, 1967, was the first Delta launch vehicle to use a digital velocity meter for determining third-stage velocity. A previous spacecraft of this series, AIMP-D, was launched into an alternate orbit rather than a lunar-anchored orbit because of a slightly high velocity attributed by some (References 1 and 2) to the third stage. The third stage, a solid-propellant rocket motor designated FW-4D (manufactured by United Technology Center), has been used as a fourth stage for Scout launch vehicles (FW-4S being the Scout version) and as a third stage for various Delta launches commencing with Delta 38 launched on May 25, 1966.

The FW-4D rocket motor was chosen because of the performance improvement expected over previously used third-stage motors, e.g., the X-258 (manufactured by Allegany Ballistics Laboratory, Hercules Co.). Third-stage velocity previously had never been determined accurately in flight. Although predictions based on static test firings indicated that the FW-4D should have had a relatively narrow range of impulse variations from motor to motor, there were no confirming in-flight measurements of sufficiently high resolution. The velocity contribution of the third stage is highly critical for the lunar-anchored AIMP orbit, and failure to deliver the required velocity necessitates either midcourse attitude correction or injection into an alternate orbit. For these reasons, a high-resolution digital output sensor was used to detect, as accurately as possible, the velocity contribution of the third stage.

This report presents the rocket performance results from third-stage telemetry instrumentation. The end instruments included an analog-type longitudinal accelerometer, a chamber-pressure gauge, and a new high-resolution digital accelerometer used as a velocity meter.

THE LAUNCH VEHICLE

Figure 1 (courtesy of Douglas Missile and Space Systems Division) is a perspective view of the launch vehicle, showing internal features of the stages in detail. Figure 2 shows the launch

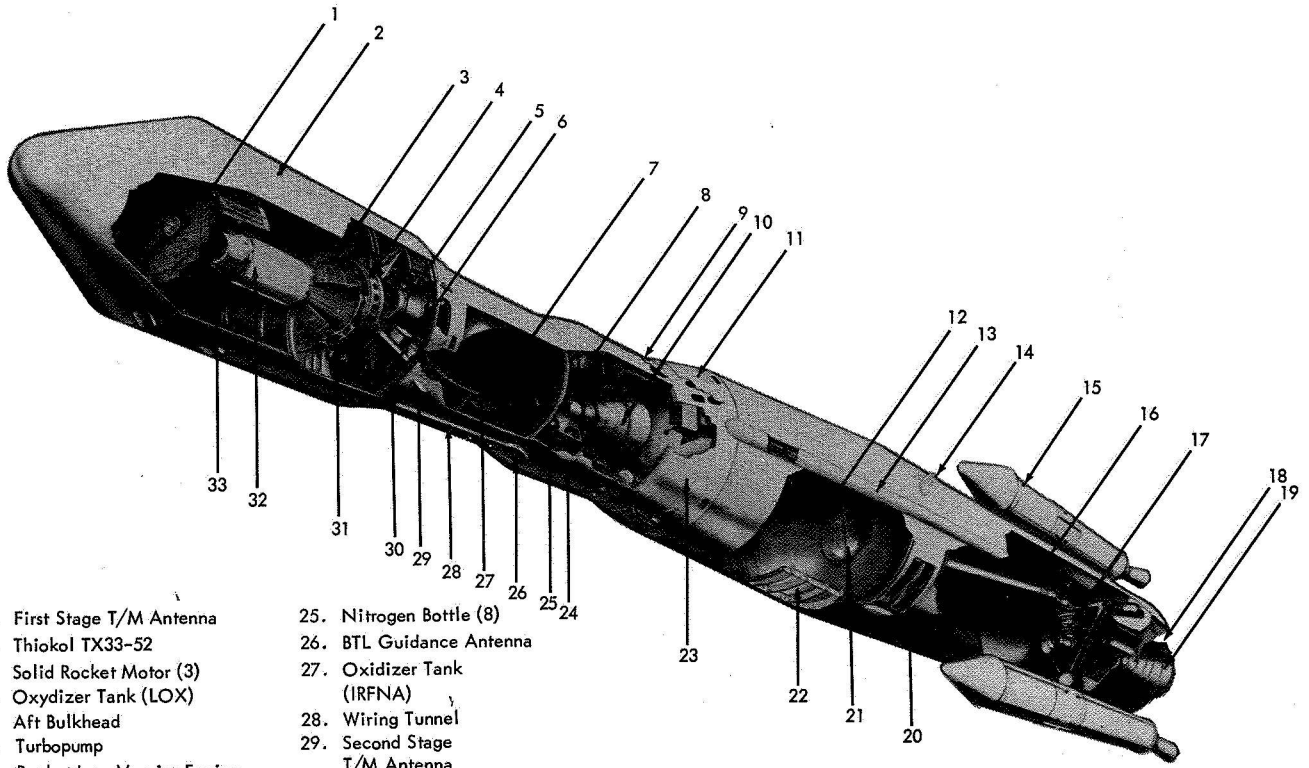

1. Spacecraft, Typical
2. Fairing
3. RF Shield
4. Spin Table
5. BTL Guidance
6. Forward Bulkhead
7. Slosh Baffles
8. Helium Bottle (3)
9. Blast Band
10. Aerojet AJ10-118E Second Stage Engine
11. Blast Band
12. Fuel Tank (RJ-1) Aft Bulkhead
13. Wiring Tunnel
14. First Stage T/M Antenna
15. Thiokol TX33-52 Solid Rocket Motor (3)
16. Oxydizer Tank (LOX) Aft Bulkhead
17. Turbopump
18. Rocketdyne Vernier Engine
19. Rocketdyne First Stage Engine
20. First Stage Telemetry
21. Anti-Vortex Baffles
22. Fuel Anti-Slosh Baffles
23. First Stage Transition Section
24. Adapter Section
25. Nitrogen Bottle (8)
26. BTL Guidance Antenna
27. Oxidizer Tank (IRFNA)
28. Wiring Tunnel
29. Second Stage T/M Antenna
30. Second Stage Guidance and Equipment Compartment
31. Spin Rocket Motor
32. FW-4D Solid Propellant Rocket Motor
33. Spacecraft Attach Fitting

Figure 1–Sectional view of Delta (DSV 3E) launch vehicle.

vehicle shortly after lift-off. The mission of Delta 50 was to launch an interplanetary monitoring platform for investigating the characteristics of the interplanetary plasma and the interplanetary magnetic field out to, and including, lunar distances. The orbit was to be either a lunar capture or a geocentric orbit with an apogee near or beyond the lunar surface. On July 19, 1967, at 10:19:02 EDT, a thrust-augmented DSV-3E Delta launch vehicle launched the spacecraft from Cape Kennedy, Florida, Launch Pad B, Launch Complex 17.

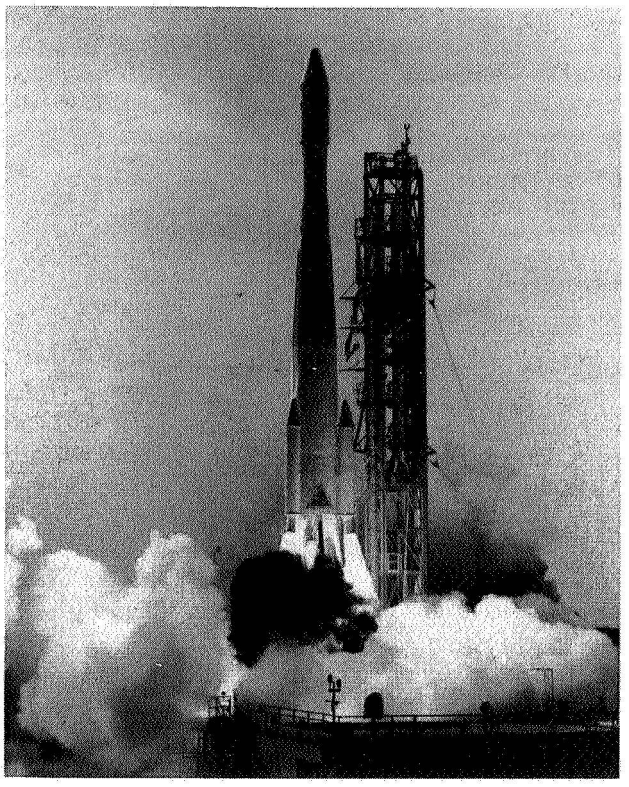

Figure 2—Launch vehicle shortly after liftoff.

Douglas Aircraft Company was the prime contractor for the launch vehicle. The first stage (S/N 20218) was a modified Thor rocket, using liquid bipropellants of liquid oxygen and a hydrocarbon fuel (RP-1) to power an MB-3 Block III Rocketdyne engine system rated at 172,000 pounds of thrust at sea level. The tankage was sufficient for a 149-second burn time. The specific impulse (I_{sp}) of the first stage was 252 seconds with a mixture ratio of 2.15:1. The first stage was augmented by three strap-on solid-propellant rockets (Thiokol TX-33-52 S/N 581, 582, 583), each rated at 54,000 pounds of thrust at sea level. The initial thrust at lift-off exceeded 330,000 pounds.

The second stage was an Aerojet General AJ 10-118E liquid bipropellant rocket rated at 7800 pounds of thrust in a vacuum; the tankage (the vehicle is sometimes referred to as the fat-tank Delta) extended the burning time to approximately 398 seconds. The propellant consisted of inhibited red fuming nitric acid (IRFNA) as oxidizer and unsymmetrical dimethyl hydrazine (UDMH) as fuel, a hypergolic propellant system delivering an I_{sp} of 267 seconds, with a mixture ratio of 2.76:1. The loaded weight was 13,030 pounds; the empty weight was 1713 pounds. The stage was 20.72 feet long; and the tankage diameter, 54.7 inches (rather than 32 inches as in the DSV-3C vehicle). The thrust chamber had an expansion ratio of 40:1 (rather than the 20:1 ratio in the DSV-3C). The second stage, like the first, was guided by two separate preprogrammed auto-pilot systems. It was also equipped with a velocity-control system to control second-stage engine cutoff.

The third stage was the FW-4D solid-propellant rocket motor (S/N 00006) manufactured by United Technology Center, a division of United Aircraft. The motor, rated at 5600 pounds thrust in vacuum with a nominal total impulse of 174,000 lb-sec in vacuum, has a burn time of 30.8 seconds and a nozzle expansion ratio of approximately 50:1. The propellant I_{sp} is nominally 285 seconds; the propellant is a solid composite (UTP 3096) of aluminum and ammonium perchlorate

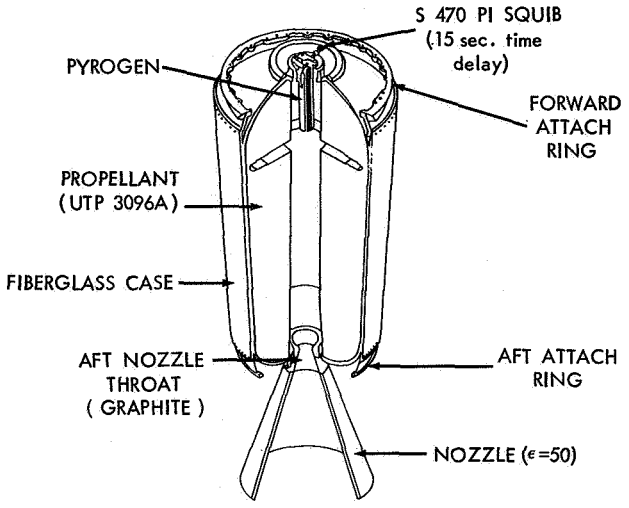

Figure 3—Sectional view of the FW-4D.

in a polyurethane base binder. The overall motor length is 58.4 inches, with a 19.6-inch diameter and a 660-pound loaded motor weight. Figure 3 is a sectional view of the FW-4D.

Ballast was added and a performance telemetry package was attached to the third stage which was mounted on a spin table and enclosed in an Improved Delta fairing (The third stage was spin-stabilized during powered flight.) Solar paddles and fluxgate booms extending from the spacecraft were folded and secured along the sides of the FW-4D motor. After third-stage burnout, the paddles and then the booms are extended, changing the spin rate from the nominal 150 rpm during third-stage burn.

THIRD-STAGE INSTRUMENTATION

The third-stage AIMP-E instrumentation package consisted of a telemetry system using three sensors: a digital-longitudinal accelerometer, an analog-longitudinal accelerometer, and a chamber-pressure gage. The telemetry system consisted of a 3-watt FM/FM transmitter radiating at 256.2 MHz, four miniaturized subcarrier oscillators for IRIG channels E, 13, 14, and 16. A mixer-amplifier, voltage regulator, two-element linearly polarized antenna, battery, control system, and umbilical completed the third-stage telemetry system.

The entire third-stage telemetry system, including end instruments, weighed just over 8 pounds. The four subcarrier telemetry channels assigned were standard IRIG channels whose

Table 1

Sensors for Telemetry System.

Function	Symbol	Location	Transducer			IRIG channel	Full-scale range	Weight (oz.)
			Model no.	Type	Output			
Longitudinal acceleration	A_D	Attach fitting	Systron-Donner 7300	Digital (servo)	(1) Pulse (2) Counter-encoder	E 14	0 to +20g	8 (combined)
Longitudinal acceleration	A_L	T/M PTM chassis	Kistler 303B	Servo	Analog	16	-4 to +16g	5
Chamber pressure	P_c	FW-4D forward dome	Bourns 725	Potentio-metric	Analog	13	0 to 800 psia	5

center frequencies were spaced sufficiently far apart to prevent introducing intermodulation errors. Miniature subcarrier oscillators were used.

Table 1 summarizes end instrumentation giving location, type of sensor, ranges covered, and weights; Table 2 lists the telemetry electronic components. Figure 4, a block diagram of the major components of the telemetry system, shows approximate instrument locations. The digital accelerometer and the chamber-pressure gauge were mounted within the attach fitting envelope between the third-stage motor and the spacecraft, whereas the longitudinal accelerometer was mounted in the telemetry chassis at the aft end of the rocket chamber. The battery box and telemetry chassis were mounted 180 degrees apart to help balance the weight of the instrumentation system about the third-stage motor. Two turnstile antennas were mounted from standoffs at the telemetry chassis and located 90 degrees apart to provide a node in the radiation pattern. This node helps detect the spin rate from the telemetry signal dropout pattern as received on the ground.

Table 2

Telemetry Electronics.

Component	Characteristics
Telemetry system	
Type	FM/FM
RF carrier frequency	256.2 MHz
Total weight	6.6 lb (exclusive of sensors)
Transmitter	
Mfr	Vector T-2125
Mode	Phase-modulated
RF power	3 watts, nominal
Antenna system	
Type	2-element, 90-degree, turnstile
Polarization	Linear
Subcarrier system	
Mfr	Vector MMD-H
A_D pulse	IRIG E 70.0 kHz
A_D counter-encoder	IRIG 14 22.0 kHz
A_L	IRIG 16 40.0 kHz
P_c	IRIG 13 14.5 kHz
Battery	
Mfr	Yardney Elec.
Type	HR-1-DC (20)
Capacity	30 milliampere-hours
Nom. drain	0.9 ampere
Life	70 minutes
Umbilical	
Type	Deutsch connector
Location	Station 138

PERFORMANCE DATA

Telemetry data from a receiving station in the Canary Islands, (27°44'N, 15°36'W) were examined for the purpose of this report.

Figure 5 is an oscillograph record of the telemetry signal after discrimination of each subcarrier signal from the RF carrier. The digital accelerometer output signal (Channel IRIG E) is shown as pulses at the top of the graph. Because of the slow paper speed (0.1 inch per second), pulses appear as a dense area; however each pulse is a measure of an integrated acceleration-time equivalent of 1 ft/sec. Next is the longitudinal accelerometer (Channel IRIG 16) signal; the vertical spikes superimposed on the analog signal represent ground-received signal dropouts. The axial accelerometer trace shows a maximum acceleration of 12.7 g's upon propellant burnout.

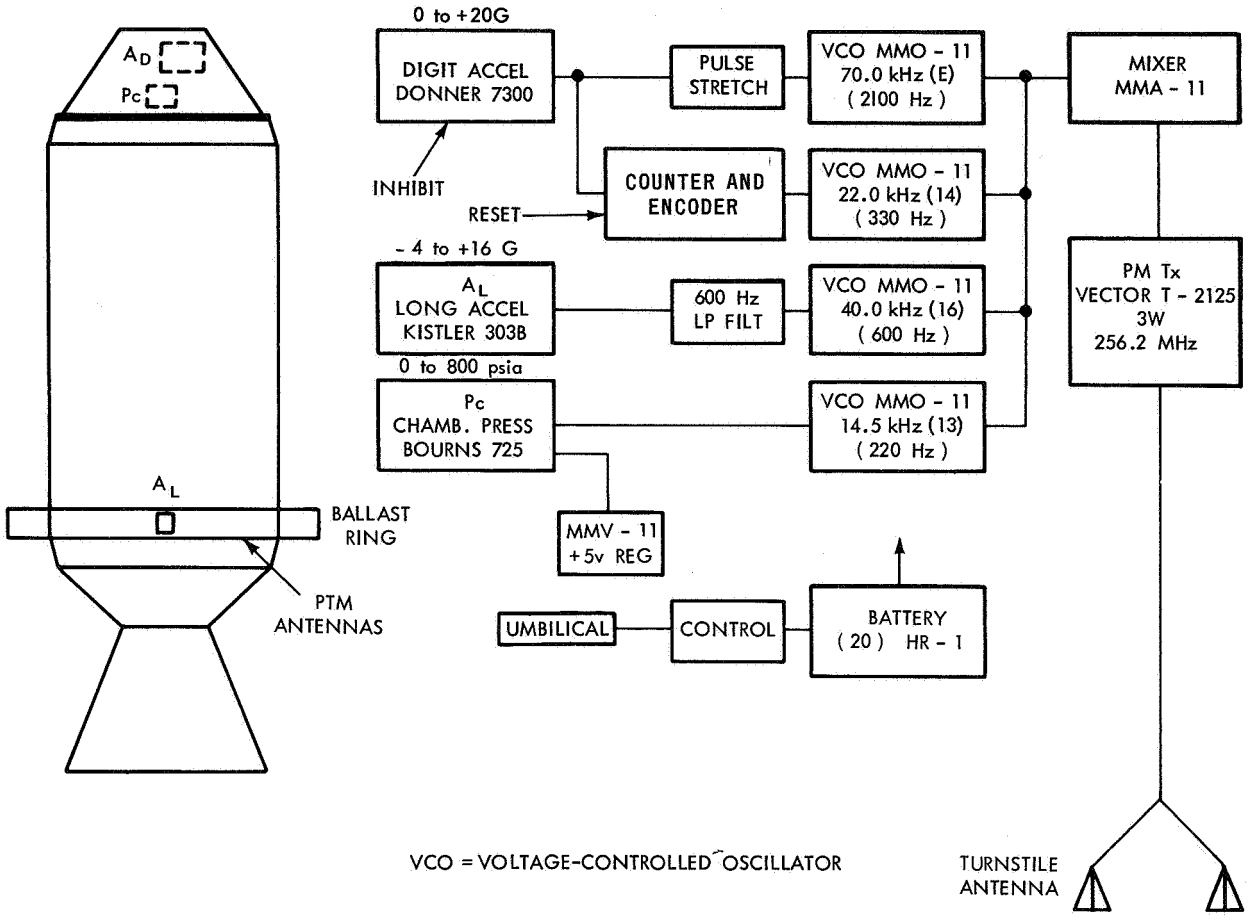

Figure 4—Major telemetry system components.

(The initial acceleration upon FW-4 ignition was 5.2 g's.) The trace indicates a nominal FW-4D acceleration-time curve. The next trace, the coded accumulated pulse count (Channel 14), appears in better perspective when displayed at faster paper speed (0.4 inch per second) (Figure 6). The coded count represents velocity attained at any time; differences show incremental velocity. The bottom curve shows the chamber pressure versus time for the FW-4D solid-rocket propellant motor (Channel 13). This chamber pressure curve can be compared with those obtained from ground static tests (References 17 and 18). The trace is typical of FW-4D chamber pressure measurements, which are characterized by a slightly pronounced hump during the first 5 seconds of burning before the peak pressure portion of the curve. The peak pressure was 775 psia, and the web burning time (t_b) was 30 seconds with a P_c of 440 psia; the full duration burn time (t_{f_b}) was 31.8 seconds.

PERFORMANCE ANALYSIS

The performance of the FW-4 third-stage motor was determined by three methods. First the chamber pressure-time curve was compared with curves from static tests made under similar

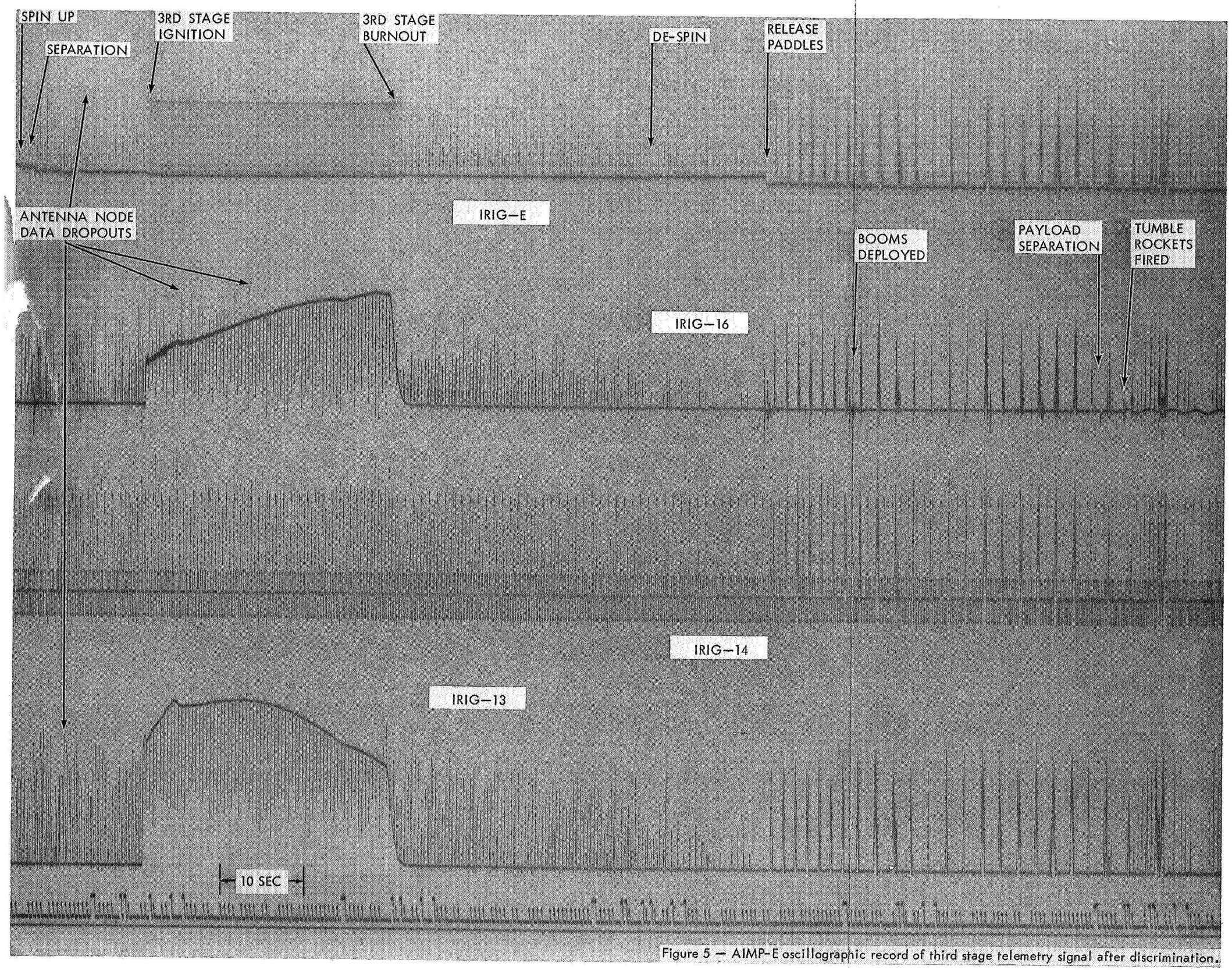

Figure 5 — AIMP-E oscillographic record of third stage telemetry signal after discrimination.

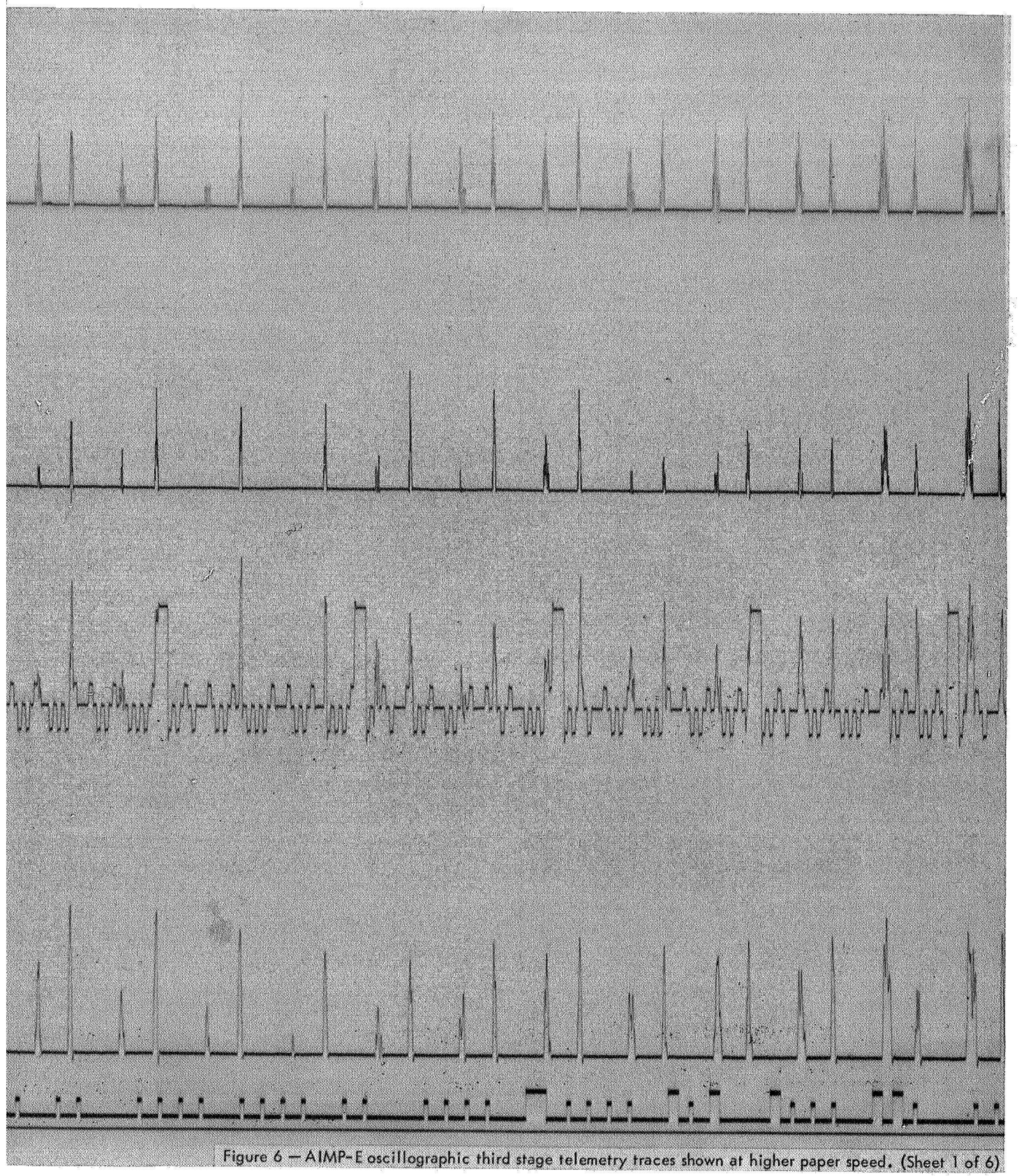

Figure 6 — AIMP-E oscillographic third stage telemetry traces shown at higher paper speed. (Sheet 1 of 6)

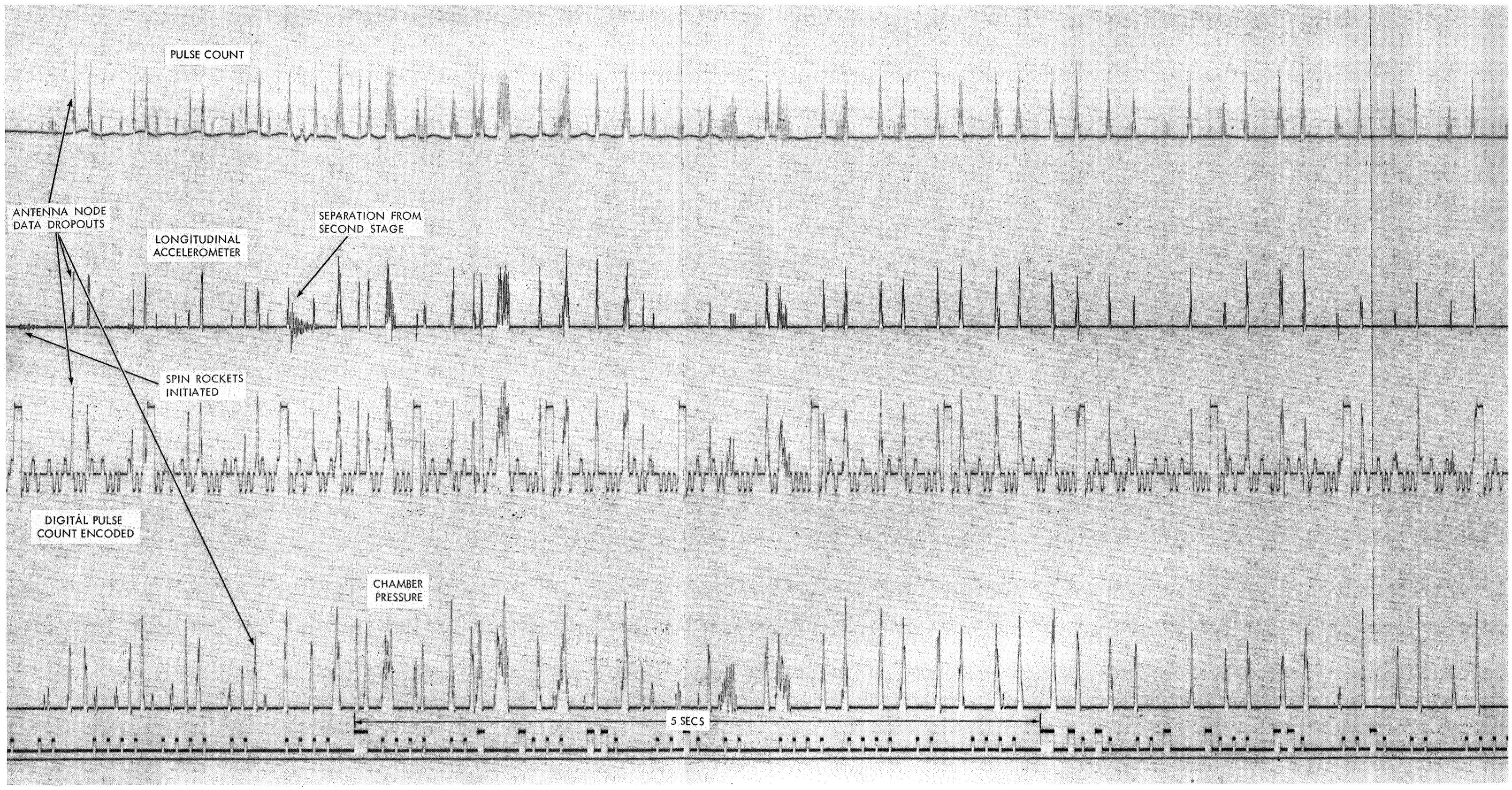
PULSE COUNT
ANTENNA NODE DATA DROPOUTS
LONGITUDINAL ACCELEROMETER
SEPARATION FROM SECOND STAGE
SPIN ROCKETS INITIATED
DIGITAL PULSE COUNT ENCODED
CHAMBER PRESSURE
5 SECS

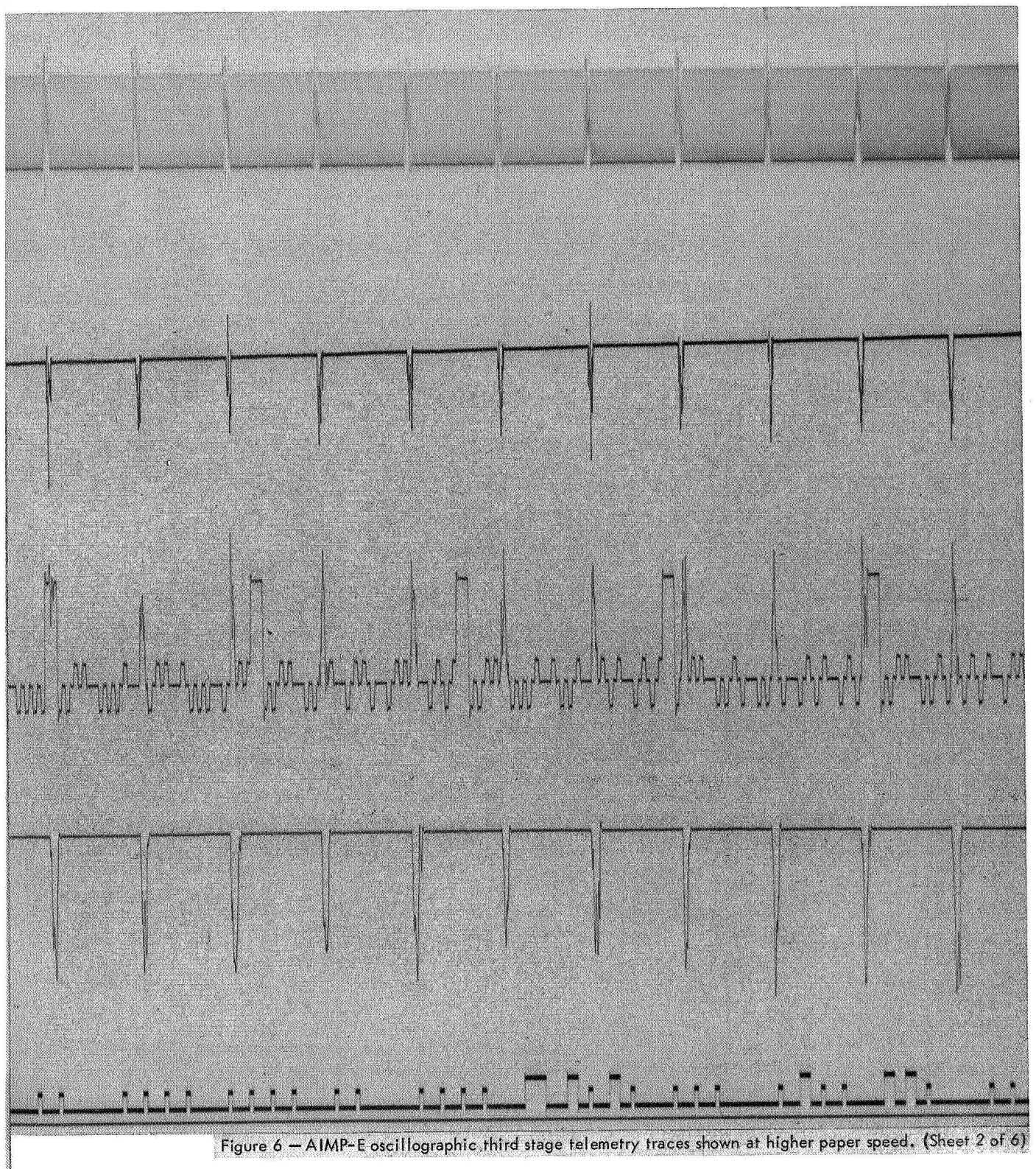

Figure 6 — AIMP-E oscillographic third stage telemetry traces shown at higher paper speed. (Sheet 2 of 6)

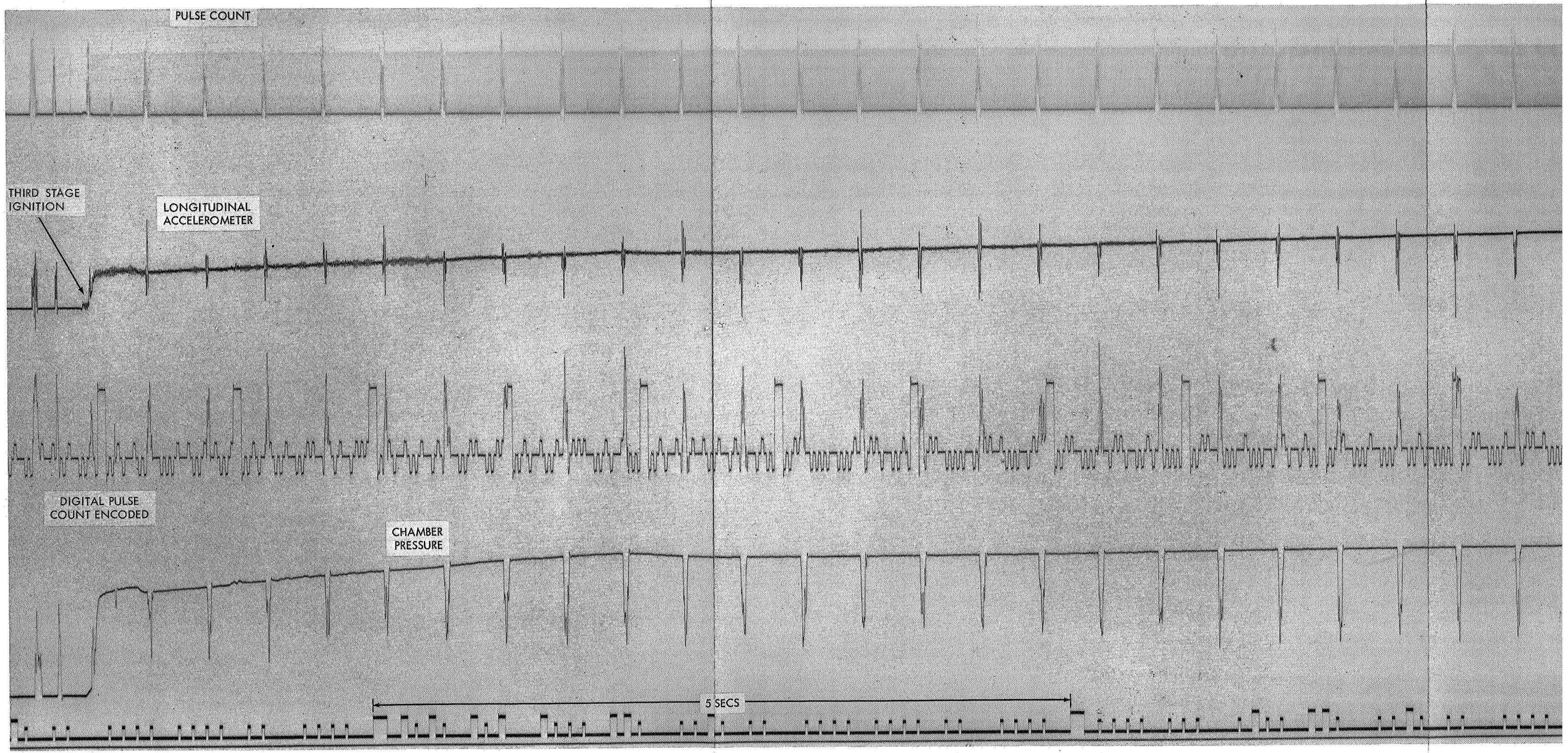
PULSE COUNT
THIRD STAGE IGNITION
LONGITUDINAL ACCELEROMETER
DIGITAL PULSE COUNT ENCODED
CHAMBER PRESSURE
5 SECS

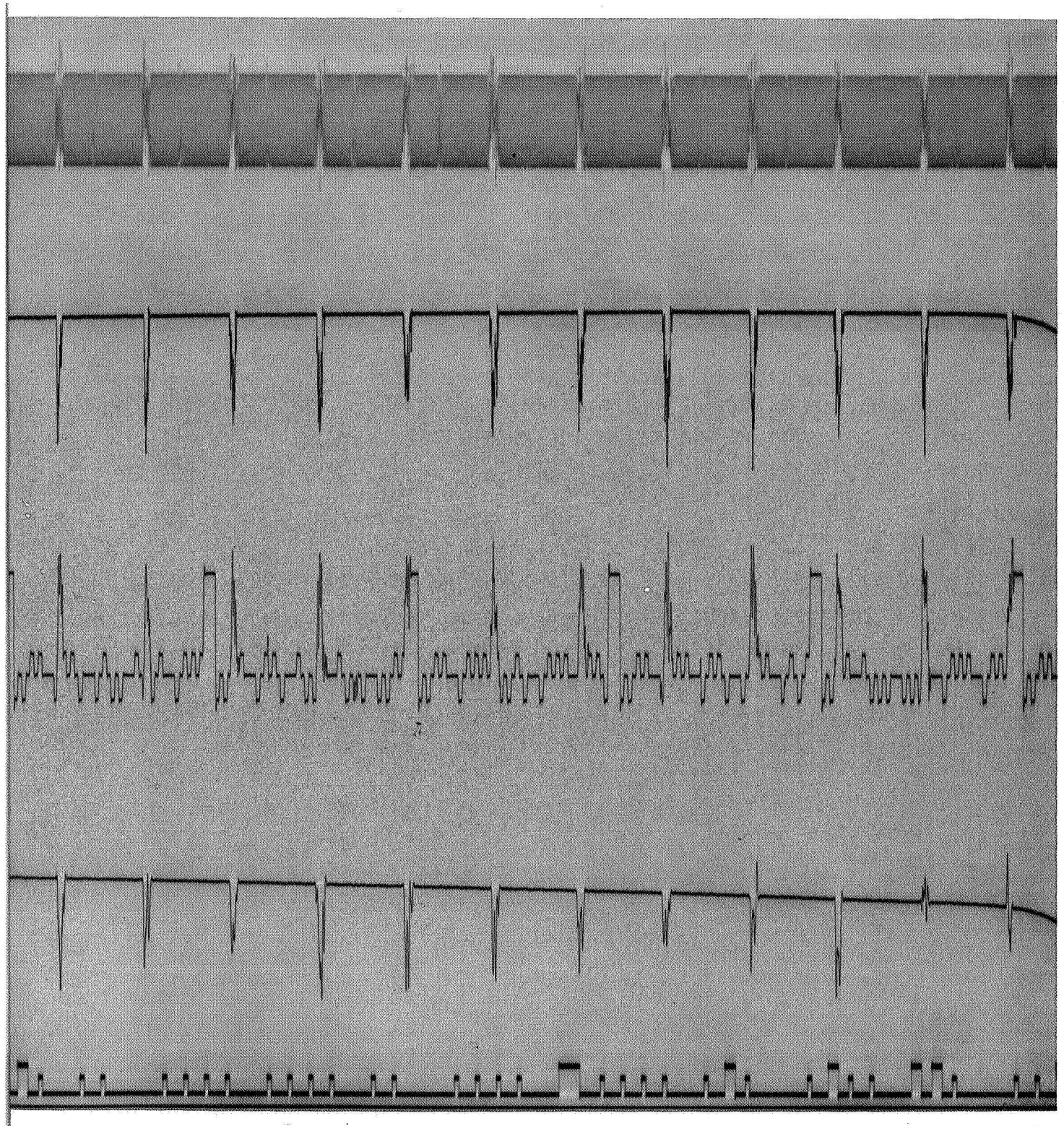

Figure 6—AIMP-E oscillographic third stage telemetry traces shown at higher paper speed. (Sheet 3 of 6)

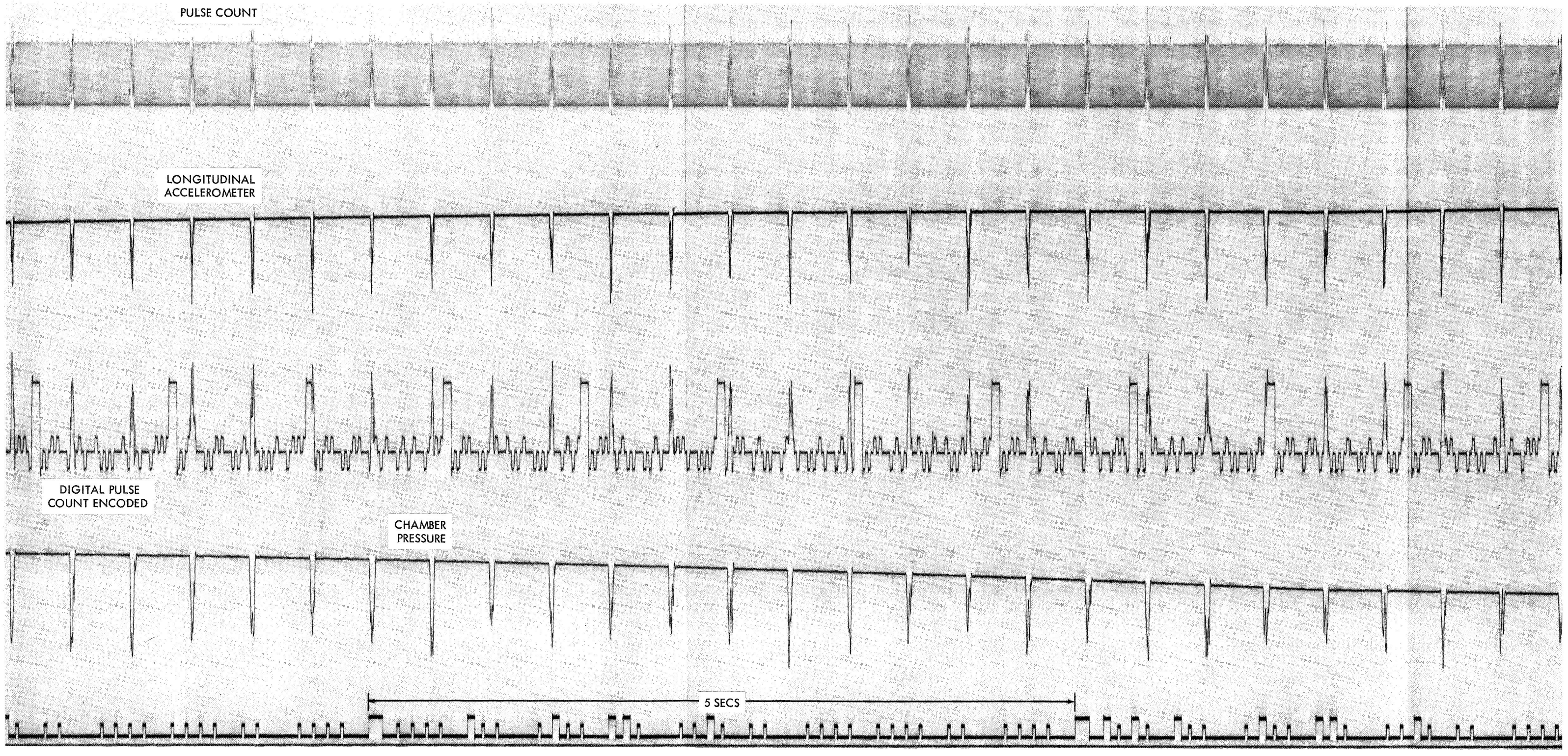
PULSE COUNT
LONGITUDINAL ACCELEROMETER
DIGITAL PULSE COUNT ENCODED
CHAMBER PRESSURE
5 SECS

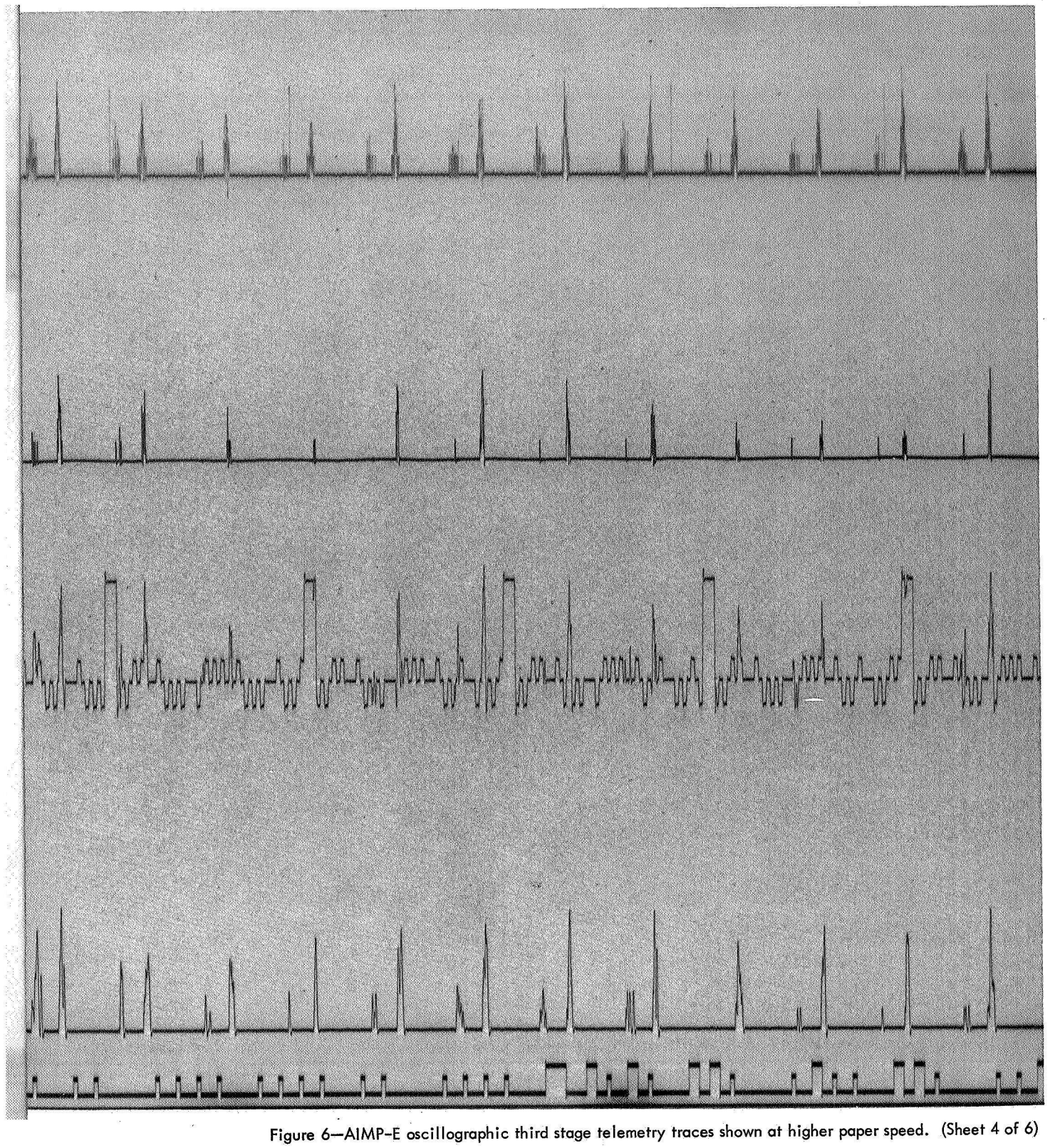

Figure 6—AIMP-E oscillographic third stage telemetry traces shown at higher paper speed. (Sheet 4 of 6)

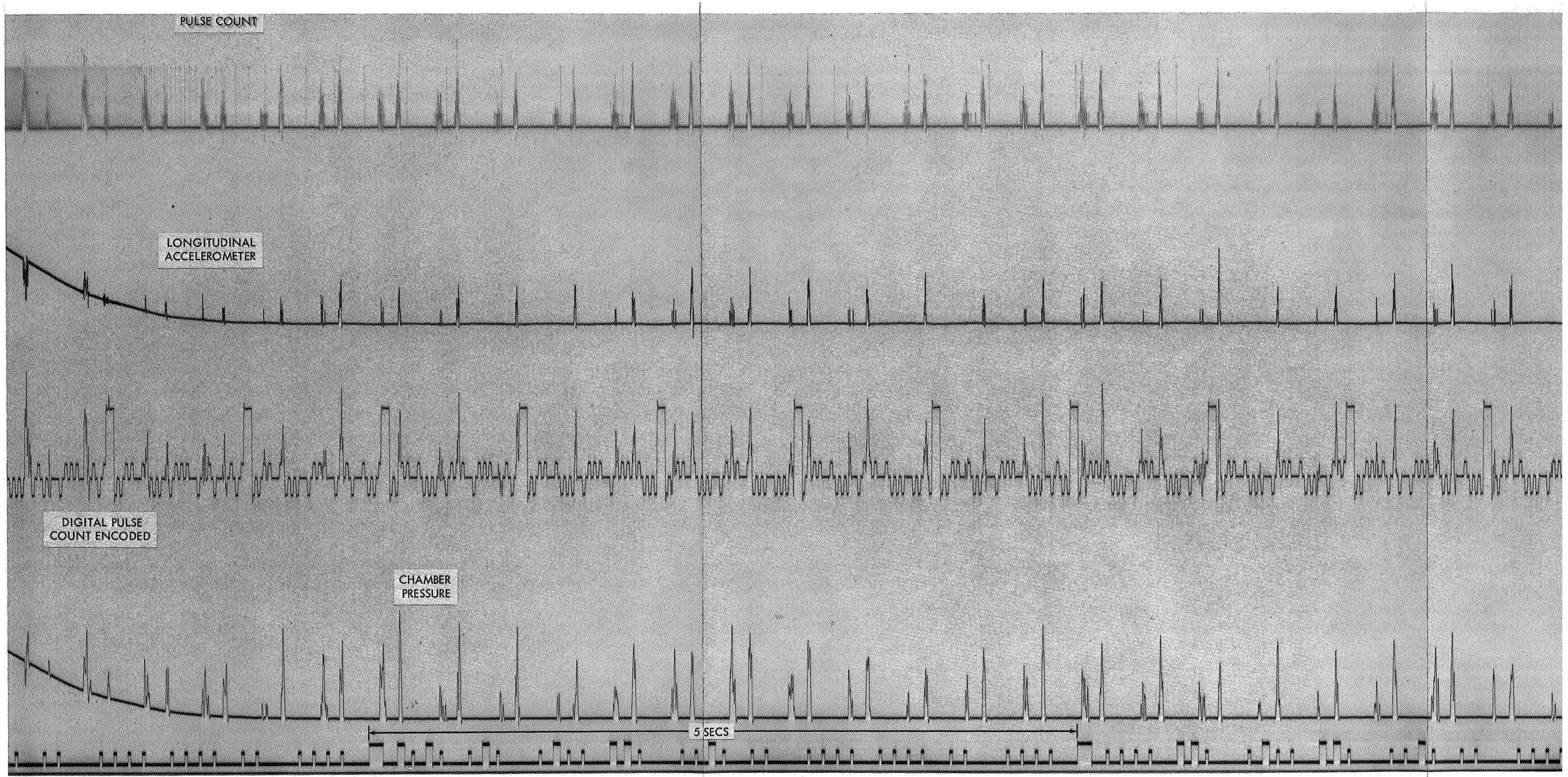
PULSE COUNT
LONGITUDINAL ACCELEROMETER
DIGITAL PULSE COUNT ENCODED
CHAMBER PRESSURE
5 SECS

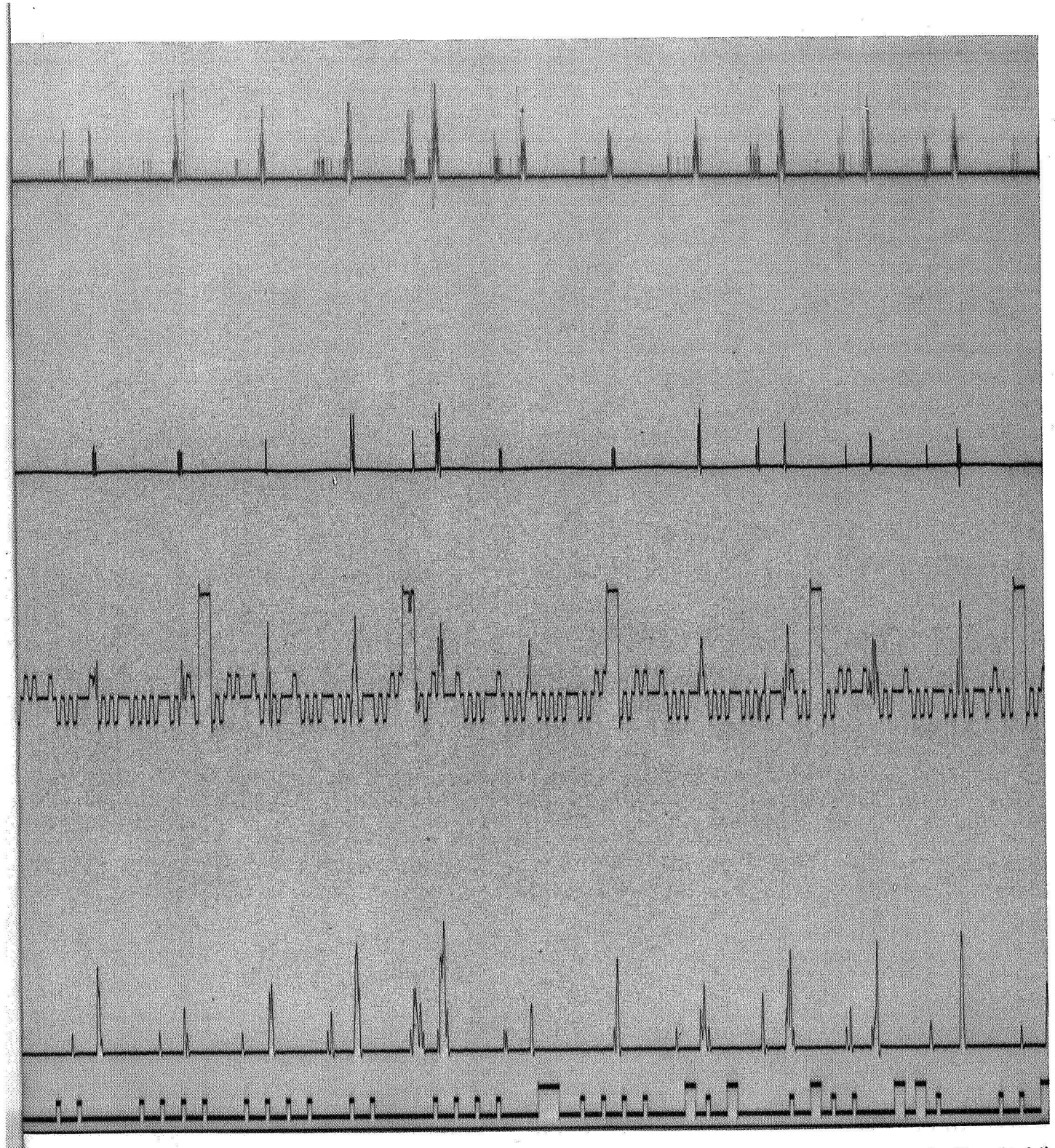

Figure 6—AIMP-E oscillographic third stage telemetry traces shown at higher paper speed. (Sheet 5 of 6)

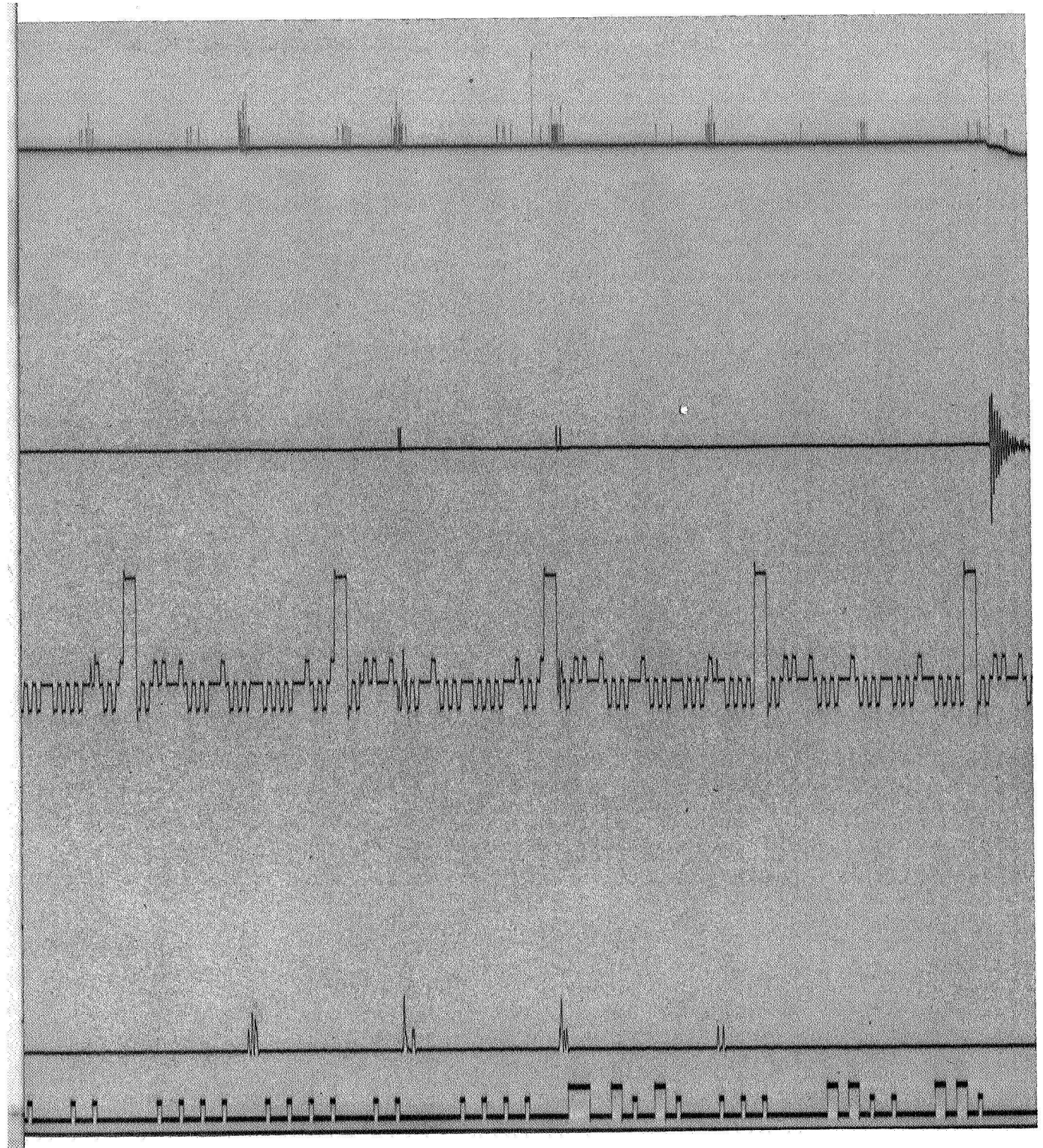

Figure 6—AIMP-E oscillographic third stage telemetry traces shown at higher paper speed. (Sheet 6 of 6)

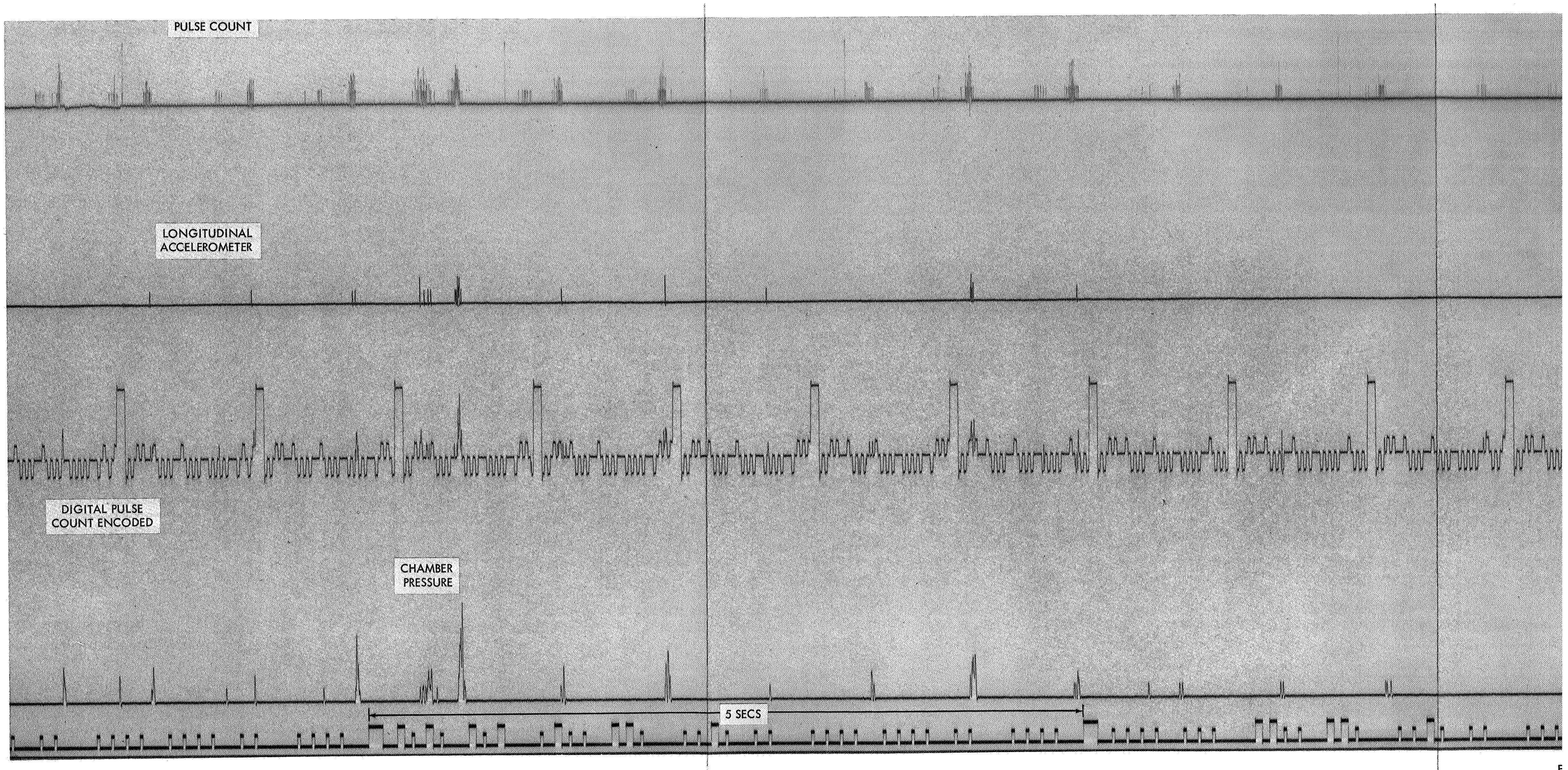
PULSE COUNT
LONGITUDINAL ACCELEROMETER
DIGITAL PULSE COUNT ENCODED
CHAMBER PRESSURE
5 SECS

F

temperature and spinning conditions; then the pressure-time curve was integrated. For reconstruction of the corresponding thrust-time curves, point-by-point pressure values were tabulated, and the corresponding thrusts calculated from conversion constants $(C_F A_t)$ derived from ground testing. Second, the longitudinal-acceleration records were inspected and the incremental velocity determined by integrating the analog acceleration-time curves. Thrust-time curves were constructed by tabulating the acceleration levels as a function of time and calculating the equivalent thrust, assuming a constant rate of propellant expenditure over the burning time (Reference 11). Third, the third-stage velocity was determined by examining the accumulated pulse count encoded from the digital longitudinal accelerometer. The pulsed output from the alternate channel was available as a backup for encoding verification. A direct count of the pulses over any time interval provided a means for troubleshooting the digital output when encoding difficulties were suspected.

Chamber Pressure

In the chamber pressure-time curve (Figure 6) the chamber pressure corresponds closely to curves obtained from ground static tests but does not show the 20-second hump obtained on Delta 38 (Reference 3). From the integrated chamber pressure-time, the effective specific impulse can be obtained from

$$k_1 I_{sp} = \frac{C_F A_t}{W_p} \int_{t_0}^{t_{f_b}} P_c \, dt \qquad (1)$$

where

k_1 = weight of propellant/total weight expended,*

C_F = thrust coefficient (dimensionless),

A_t = area of throat in square inches,

$\int_{t_0}^{t_{f_b}} P_c \, dt$ = integrated pressure-time curve over the full duration burn time in psia-seconds,

$k_1 W_p$ = weight of propellant in pounds, and

W_p = weight expended in pounds.

The propellant specific impulse can then be obtained from

$$I_{sp} = \frac{C_F A_t \int_{t_0}^{t_{f_b}} P_c \, dt}{k_1 W_p}, \quad \text{sec.} \qquad (2)$$

*k_1 need not be 1.00 inasmuch as some inert material is generally expended during burning.

The integrated $P_c\,dt$ curve yielded a value of 20,540 psia-sec (for Delta 50) which, substituted into Equation 1 produces an I_{sp} of 282.1 seconds and an effective specific impulse ($k_1 I_{sp}$) of 280.0 seconds. The total impulse may then be calculated from

$$Ft = k_1 W_p I_{sp} = C_F A_t \int_{t_0}^{t_{f_b}} P_c\,dt \,. \tag{3}$$

Using the weights listed in Appendix D, we obtain for the total impulse 171,500 lb-sec.

Longitudinal Acceleration

The longitudinal-acceleration curve (Figure 6) corresponds closely to the chamber-pressure curve; i.e., there are matching deflections for every peak and valley. The acceleration-time curve shows a continually rising amplitude, accounted for by the nearly linear propellant mass depletion. The acceleration-time curve was integrated, and the area was found to be 299.3 g-sec. Using

$$v = \int_{t_0}^{t_{f_b}} a\,dt \,, \tag{4}$$

the velocity was found to be 9630 ft/sec at the end of burning. Peak acceleration was found to be 12.7 g's at 28.5 seconds after ignition. A slight coning motion is detectable both before third-stage ignition and after burnout. Inspection of the oscillatory nature of the acceleration-time curve during those periods reveals that the ripple was not merely instrumental error, since no ripple was present before third-stage ignition. Furthermore, after boom deployment, the period of the oscillation changes, corresponding to a change in the spin rate.

Velocity

The incremental velocity imparted by the FW-4D motor was determined by three methods. First, the third-stage velocity was measured directly from the incremental velocity pulse count of the digital longitudinal accelerometer. Second, it was calculated from the value of incremental velocity found from integrating the analog longitudinal accelerometer curve. Third, it was calculated from the chamber pressure-time curve integration. A direct measure of velocity can be obtained from the digital integrating accelerometer which is displayed in two forms—pulse count and pulse frequency.

The pulse count is displayed in Figure 7 according to the encoding procedure described and shown in Figure 8. Since the pulse count is shown as an accumulated count, and a 1-second marker is applied per frame, each successive encoded word shows the velocity increase in that

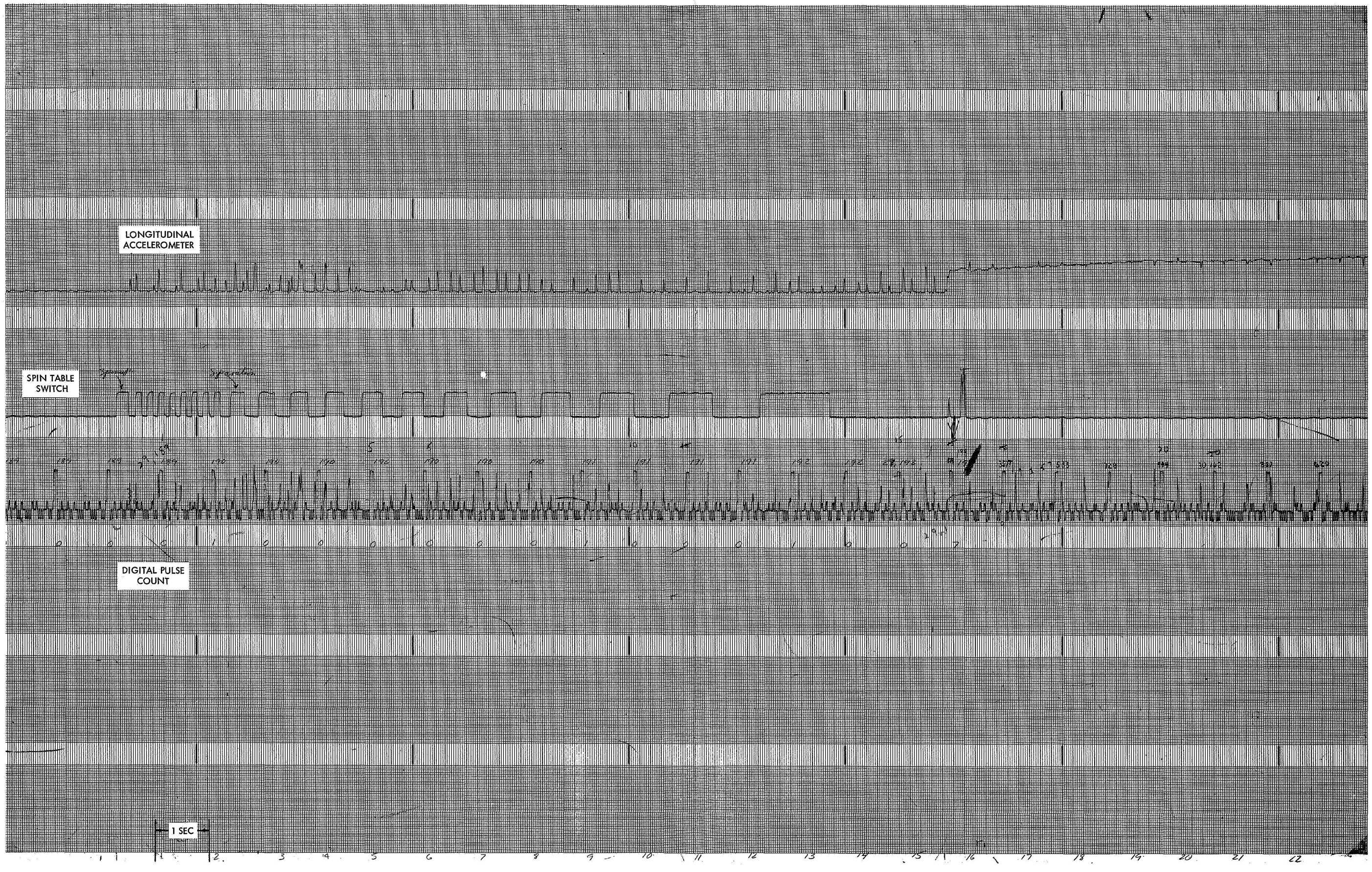

Figure 7—Sanborn oscillographic display. (Sheet 1 of 4)

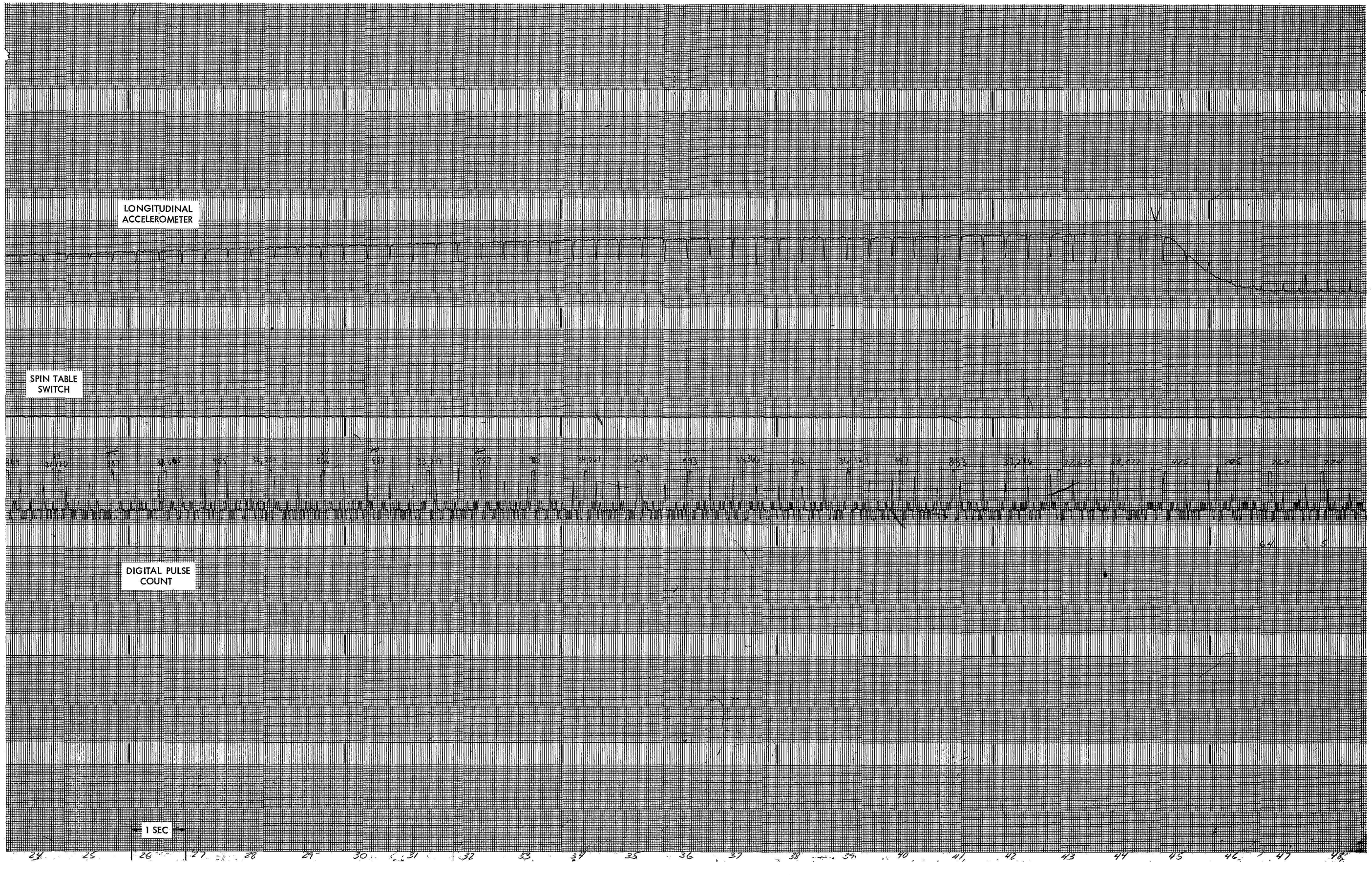

Figure 7—Sanborn oscillographic display. (Sheet 2 of 4)

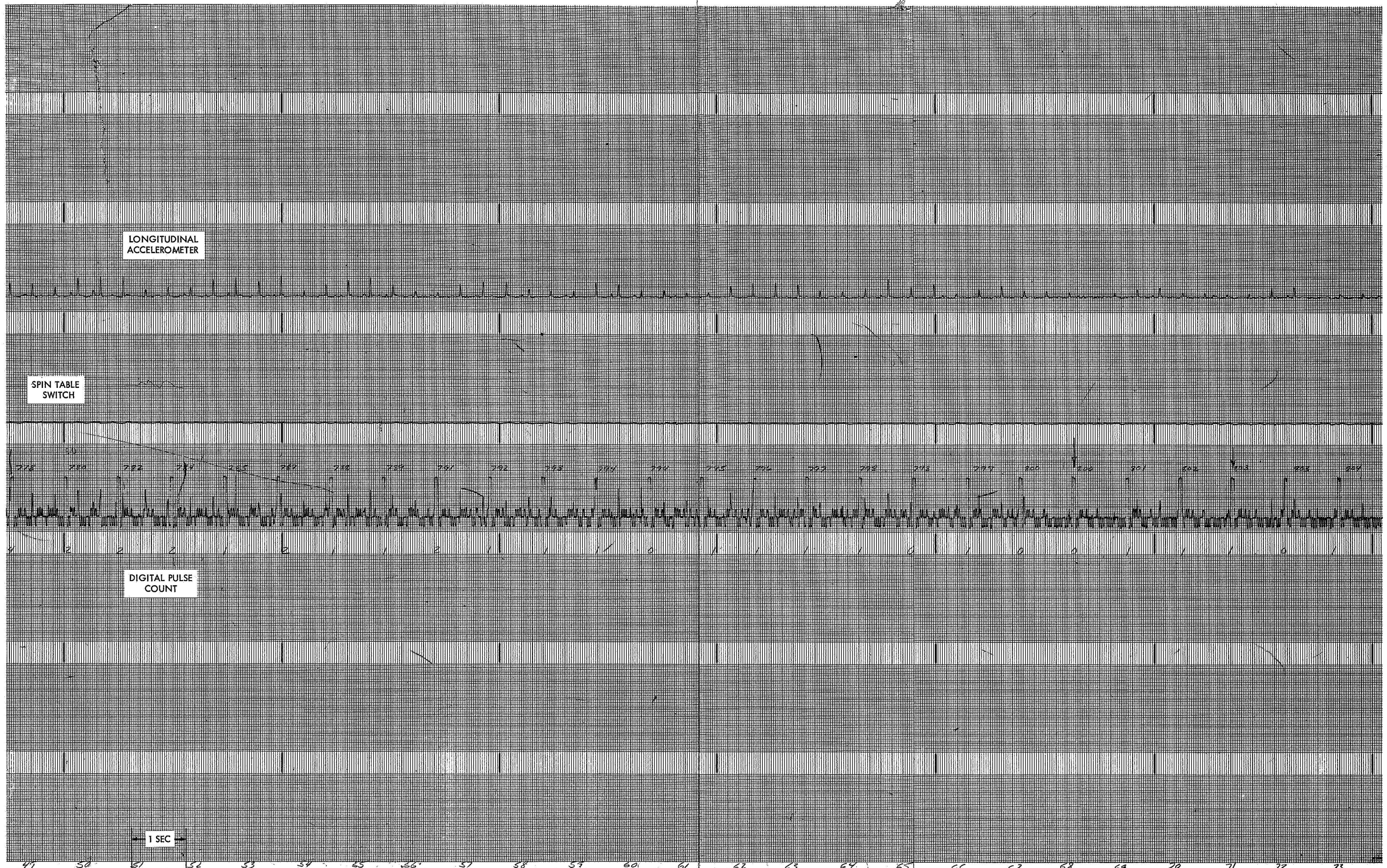

Figure 7–Sanborn oscillographic display. (Sheet 3 of 4)

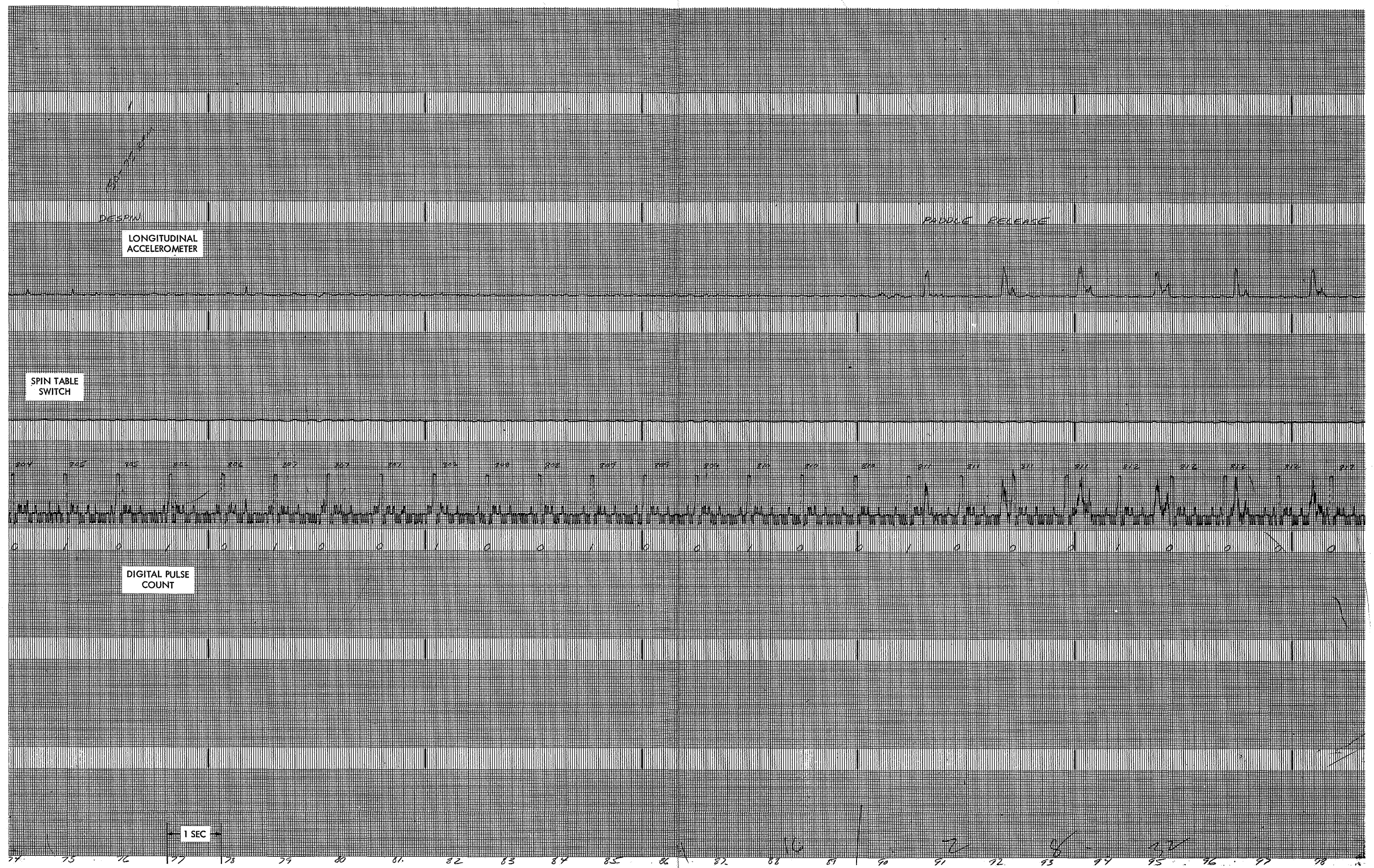

Figure 7–Sanborn oscillographic display. (Sheet 4 of 4)

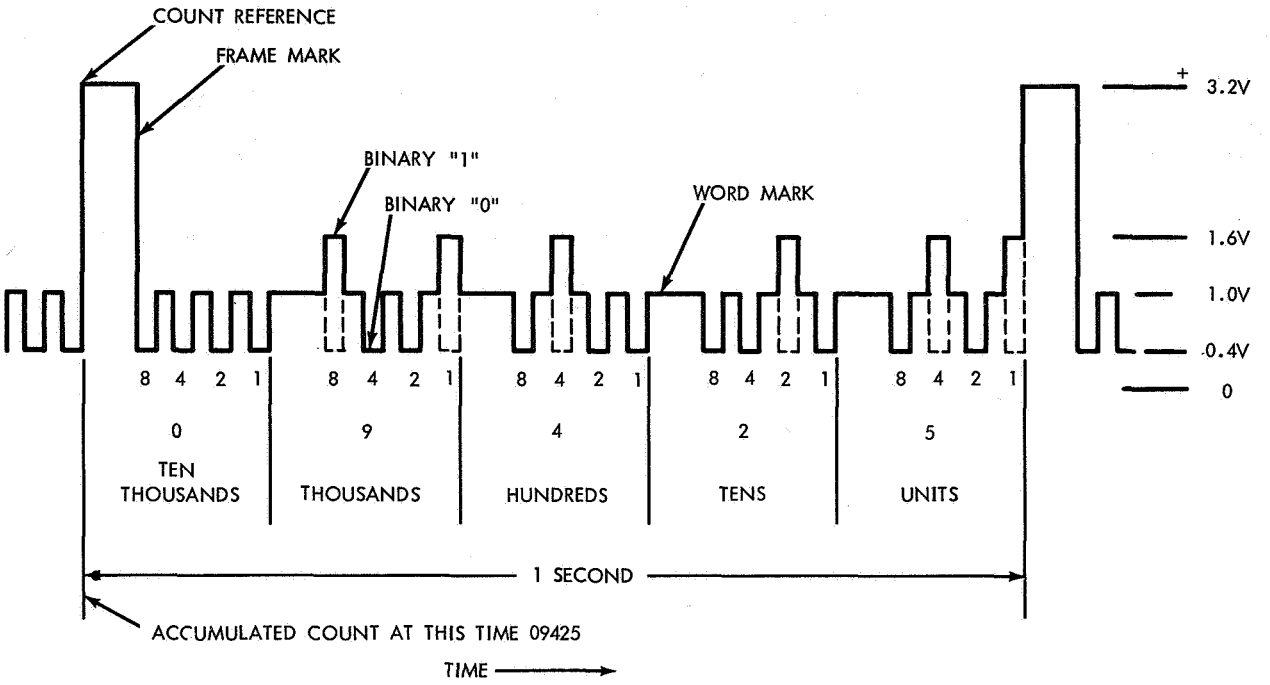

1 - 2 - 4 - 8 BINARY CODE
MOST SIGNIFICANT BIT IS READ OUT FIRST
VOLTAGE LEVELS ± 5%
FRAME PERIOD: 1 SECOND ±10%

Figure 8—Digital accelerometer accumulated count code format.

time interval, namely time-integrated acceleration directly. Before launch, the accelerometer was adjusted to deliver 32.2 pulses per second under 1-g acceleration; thus each pulse represents 1/32.2 g-sec. or 1 ft/sec. During the period between spinup and third-stage ignition (a period of 15.3 seconds), three pulses were detected, which would correspond to an axial velocity increase of 3 ft/sec. Since the longitudinal accelerometer record shows that some coning occurred during this period, the 3 ft/sec was attributed to the spin component in the axial direction, an error caused by the high-resolution capability of the digital accelerometer in the axial direction. Between the onset of ignition and burnout, a pulse count of 9582 (38774-29192) was obtained, corresponding to 9582 ft/sec. From the plot of pulses continuing after burnout (Figure 9), it can be seen that an additional 28 ft/sec occurs beyond that which can be attributed to coning. Therefore, the final incremental velocity from the third stage was 9610 ft/sec for the accumulated pulse count.

The pulse count was arrived at by determining the terminal-digital count that represented the final velocity and then by subtracting the digital count at the time of third-stage ignition. The velocity component in the axial direction caused by pre-ignition coning can be determined during the period between spinup and ignition. From the pulse count, the incremental velocity was found to be 9582 ft/sec at 48 seconds after the firing signal. The time delay from firing signal to ignition was 15.3 seconds; therefore, the velocity of 9582 ft/sec corresponds to third-stage burnout

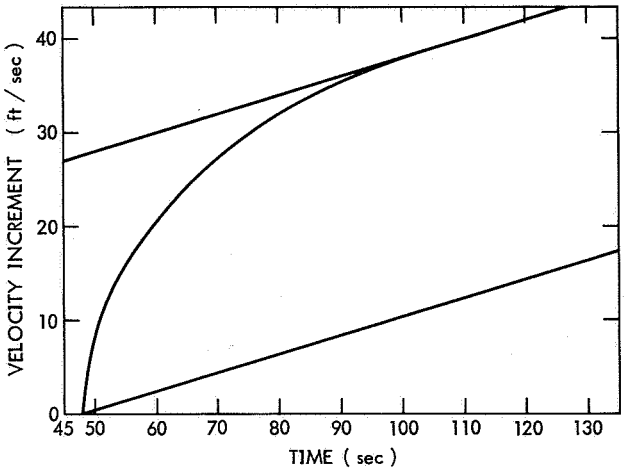

Figure 9—Third-stage velocity increment after burnout.

tail-off conditions. The velocity at +52 seconds past burnout was 9610 ft/sec and did not appear to rise further within the resolution (1 ft/sec) of the end instrument.

From the incremental velocity, the effective specific impulse can be calculated from

$$k_1 I_{sp} = \frac{\Delta V}{g \ln (W_0/W_f)} , \qquad (5)$$

where

ΔV = incremental velocity = 9582 ft/sec at burnout, 9610 ft/sec at 52 seconds post burnout,

g = gravitation constant = 32.174 ft/sec^2,

W_0 = stage III ignition weight = 936.8 lb., and

W_f = stage III burnout weight = 324.80 lb.

Using the foregoing spacecraft weight values, effective specific impulses were calculated as shown in Table 3.

No attempt was made to reduce the pulse-frequency signal by direct count during the burning period because of the high pulse rate during each time interval (approximately 300 pulses per second). However, the number of pulses after burnout was compared with the accumulated digital-pulse count. Figure 7 shows the pulses and their counterpart, the accumulated pulse count. Because agreement was found during all intervals inspected, it was concluded that the pulse counter and digital encoder were in agreement and therefore were functioning properly. The pulse-frequency

Table 3

Comparison of Instrumental Results.

Source	ΔV	Effective $k_1 I_{sp}$		I_{sp}		Total Impulse lb-secs
		At burnout	At separation	At burnout	At separation	
Pressure	9538	280.0	280.0	282.1	282.1	171,500
Long. acc.	9630	282.6	282.6	284.7	284.7	173,000
Digital Acc.	9582 9610	281.2	282.0	283.3	284.1	172,100 172,600

display was intended solely for troubleshooting applications; however, no troubles were encountered, and the accumulated pulse count, as encoded, was used for the direct determination of incremental velocity.

The longitudinal accelerometer used to determine analog acceleration was a servo-type Kistler 303B rated for a range of 20 g's, delivering one-fourth volt per g or 5 volts full scale. The accelerometer was offset to read from -4 g to +16 g for a 0- to 5-volt full scale (Appendix C).

The chamber pressure-time curve was integrated, yielding an area of 20,540 psia-seconds. Using

$$\Delta V = g\, k_1\, I_{sp}\, \ln \frac{W_0}{W_f} \tag{6}$$

combined with

$$g\, k_1\, I_{sp} = \frac{C_F\, A_t}{W_p} \int_{t_0}^{t_{f_b}} P_c\, dt \tag{7}$$

gives

$$\Delta V = \frac{C_F\, A_t}{W_p} \int_{t_0}^{t_{f_b}} P_c\, dt\, \ln \frac{W_0}{W_f}\ , \tag{8}$$

from which we can calculate the velocity corresponding to the total impulse derived from the pressure-time curve. A conversion factor from ground static tests for $C_F\, A_t$ is assumed (Figure 10). This assumption implies that the throat-erosion behavior is the same as that obtained in ground testing. The pressure-time curve is not a direct, but a derived measure of velocity that depends on the thrust axis being true with respect to the longitudinal axis. Any thrust misalignment introduces an error; and any variation in throat erosion, nozzle over-erosion, or expansion ratio from that obtained in static tests would also show up as an error. Thus, the pressure-derived value calculated for velocity has the lowest inherent accuracy.

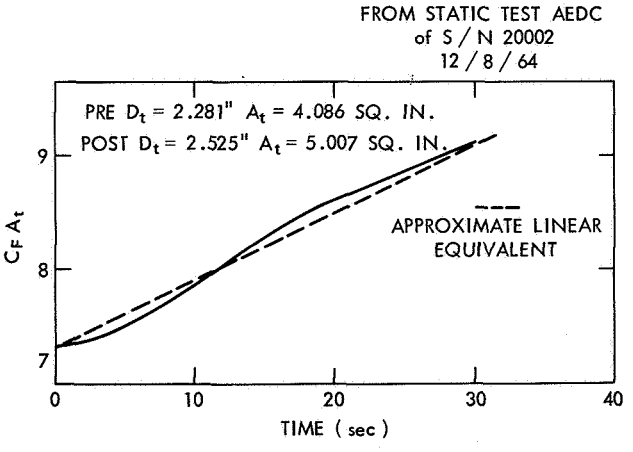

Figure 10—Results of $C_F A_t$ ground static tests.

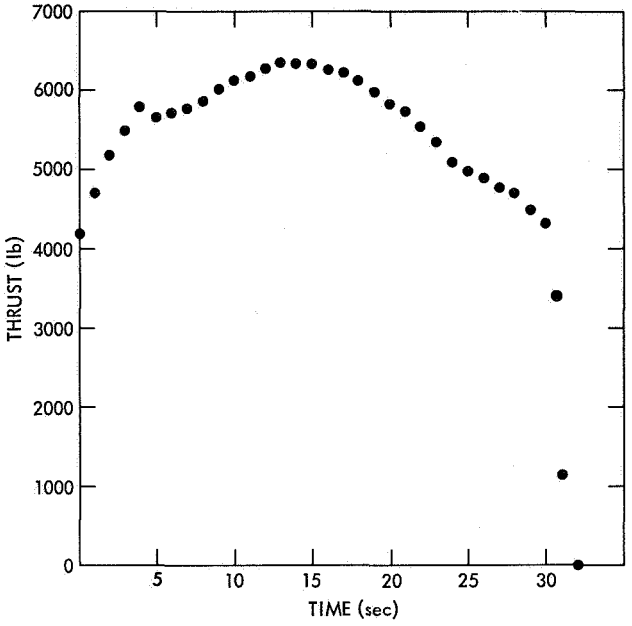

Figure 11a—Thrust-time curve reconstructed from telemetered chamber pressure.

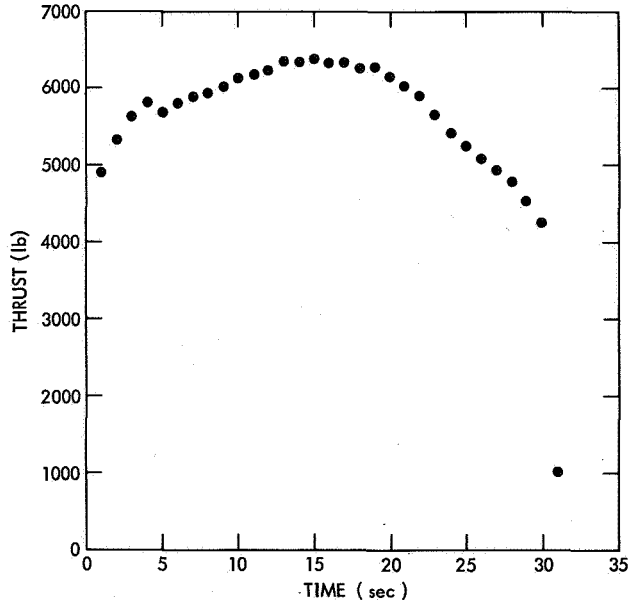

Figure 11b—Thrust-time curve reconstructed from longitudinal accelerometer records.

Reconstructed Thrust-Time Curves

Three thrust-time curves were constructed from the end instrument measurements: chamber pressure, longitudinal accelerometer, and digital accelerometer. Figure 11a shows the thrust-time curve constructed by applying

$$F = C_F A_t P_c \qquad (9)$$

and calculating thrusts from the telemetered pressure values as a function of time. The values of $C_F A_t$ were taken from Figure 10, obtained from a test firing under simulated high-altitude conditions (Reference 2).

Figure 11b is the thrust-time curve generated from the longitudinal-accelerometer records using

$$F = ma \ , \qquad (10)$$

where

m is the instaneous mass derived by assuming a constant rate of propellant depletion; thus

$$m = m_0 - \dot{m}\Delta t \ , \qquad (11)$$

where

Δt is the time interval (seconds) from ignition and

$\dot{m}$ is the constant-mass rate of propellant expenditure in slugs per second.

In assuming constant-mass flow rate, the derived thrust-time curve is subject to a slight error that could be alleviated by introducing a variable-mass flow-rate term. However, the agreement between pressure-derived and acceleration-derived thrust-time curves is so close that further correction is hardly warranted.

Figure 12 is the thrust-time curve calculated from the digital-accelerometer measurements using accelerations based on 1-second increments. Thrust was calculated from Equation 10 ($F = ma$), using the same instantaneous mass values as those for the longitudinal-acceleration calculation. Thrust calculated in this manner requires a measurement of the acceleration that, in turn, is derived from the velocity over the preceding 1-second interval. Therefore, this value lags during changing velocities and tends to smooth out rapid variations in thrust. This effect is more easily discernible by comparing the three constructed thrust-time curves in detail (see Figure 13). The agreement for all three curves, considering the various potential sources of error, is remarkably good.

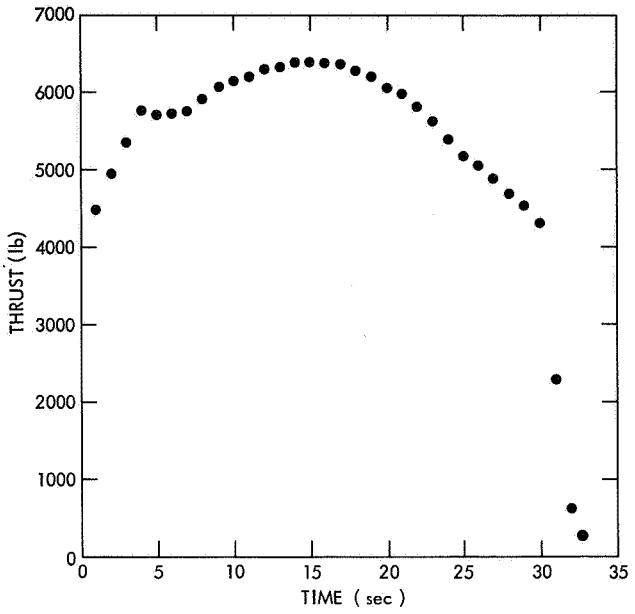

Figure 12—Thrust-time curve reconstructed from digital accelerometer measurements.

Propellant Specific Impulse

Propellant specific impulses based upon the manufacturer's stated propellant weight and an estimated weight loss of 4.5 pounds of consumed inert weight are shown in Table 3. The effective specific impulses are also listed. The velocity meter is the superior instrument for establishing incremental velocity, and therefore provides the most accurate value for I_{sp}. Both pressure and longitudinal-accelerometer measurements are in close agreement, the longitudinal accelerometer being slightly high, pressure measurement being low, but both being in I_{sp} agreement to ±1.4 second or within ±1/2 percent. However the digital accelerometer detected an increase in specific impulse during the post-burnout period. Longitudinal-accelerometer and pressure transducers were unable to discriminate any such low-level effect.

The area found by integrating the $P_c\ dt$ curve agreed with values obtained from static tests. The effective specific impulse calculated from pressure agrees within 1 percent with the figures calculated from incremental velocities.

Spin Rate

Third-stage spin rate was calculated from telemetry signal dropouts attributable to nodal points in the radiated pattern from the antenna configuration. Spin rate was slightly less than the nominal 150 rpm: 140.4 rpm at third-stage ignition and increasing to 146.4 rpm at burnout.

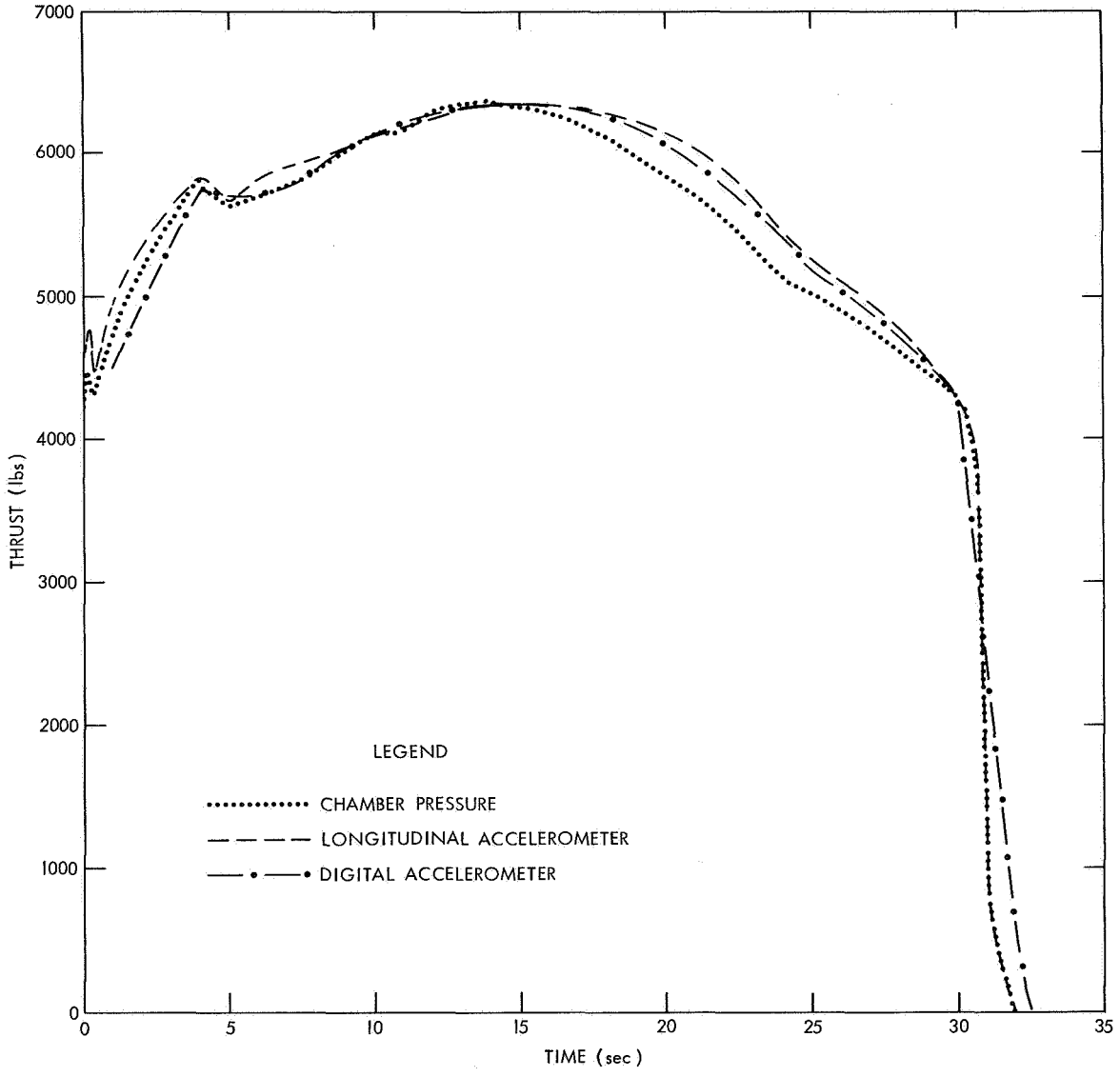

Figure 13—Comparison of thrust-time curves.

Outgassing

Velocity (as detected by pulse count) continues to rise after burnout (Figure 7). If we postulate that the spin-component contribution to the axial acceleration remains constant, this contribution can be ascertained from an inspection of the pulse count during the spin period well after third-stage burnout. Figure 7 indicates that this pulse count reaches a constant slope of about 3 ft/sec over a 15-second period, or 0.2 ft/sec/sec or 0.006 g. Therefore, subtracting this contribution over the period from tail-off of third-stage burning until the same level is approached near separation provides the net velocity attained after burnout. From the plot of the net forward velocity with time (Figure 9) the continued velocity rise, presumably caused by outgassing, can be detected. Since a velocity rise of about 1 ft/sec (the limit of resolution of the digital accelerometer) is still being detected until about 100 seconds from third-stage spinup (52 seconds after burnout), the third-stage motor must still be generating some thrust. Thus, from 48 to 100 seconds after spinup, a velocity increment of 38 ft/sec was noted, of which 10 ft/sec could be attributed to error from the spin contribution, leaving an increase of 28 ft/sec from other causes, presumably outgassing.

DISCUSSION OF INSTRUMENTS

Digital Accelerometer-Type Velocity Meter

A digital accelerometer (Model 7300 manufactured by Systron-Donner Corporation) was used as a velocity meter. This instrument uses a high-resolution servo-type accelerometer but replaces the usual load resistor with a precision capacitor. The current used for restoring the seismic mass upon acceleration charges a precision capacitor at a rate proportional to the detected acceleration. While the capacitor is being charged, its voltage is compared with a reference voltage. As soon as the reference voltage is exceeded, an output pulse is triggered. Each output pulse represents the time integral of acceleration in g-seconds and, therefore, is a direct measurement of incremental velocity.

The Systron-Donner Model 7300 is adjusted to send forth 32.2 pulses per second under 1-g acceleration. Each pulse therefore represents an incremental velocity of 1 ft/sec or 1/32.2 g-sec (0.031 g-sec). The series of output pulses can then be sent to a counter or accumulator, which then displays the total number of pulses. The difference between accumulated pulse count at any time and a subsequent time constitutes the incremental velocity during that period. The Model 7300 has a very low sensitivity to side-force accelerations and senses acceleration only in the axial direction. The high resolution of the accelerometer can easily be offset by introducing coning errors detected in the axial direction; therefore the accelerometer case must be aligned accurately with respect to the spacecraft axis to reduce the potential error caused by off-center mounting.

Figure 14 shows the relationships between waveforms for an acceleration-time curve, its velocity counterpart (namely the integrated acceleration-time curve, or velocity-time curve) the

capacitor-charge time curve, and the pulse-time frequency curve. A simplified block diagram of the electronics package is shown in Figure 15. The normal output pulse of the digital accelerometer is only 10 microseconds in duration. For this reason, incorporation of a "pulse stretch" (Figure 4) was necessary to permit transmission of the pulsed signal on a standard voltage-controlled oscillator. The pulse stretch provides a pulse width of approximately 300 microseconds, enabling normal ground-station recording and display equipment to handle the data with conventional ground-station equipment. Figure 8 shows the coded accumulated pulse count format. A binary-coded-decimal format is used with a reference pulse for a frame marker. Five 4-bit words cover an accumulated count to 99,999, giving potential resolution to 1 part in 100,000. Inverting a pulse encodes in binary format the units, tens, hundreds, thousands, and ten-thousands place for the count encoding, accumulated count information.

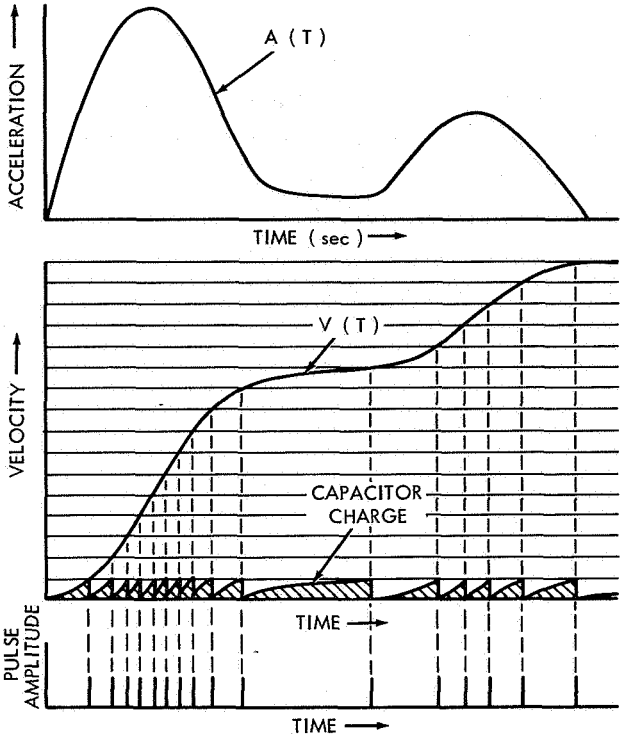

Figure 14—Waveform relationships for Model 7300 digital accelerometer, showing pulse frequency versus acceleration and velocity.

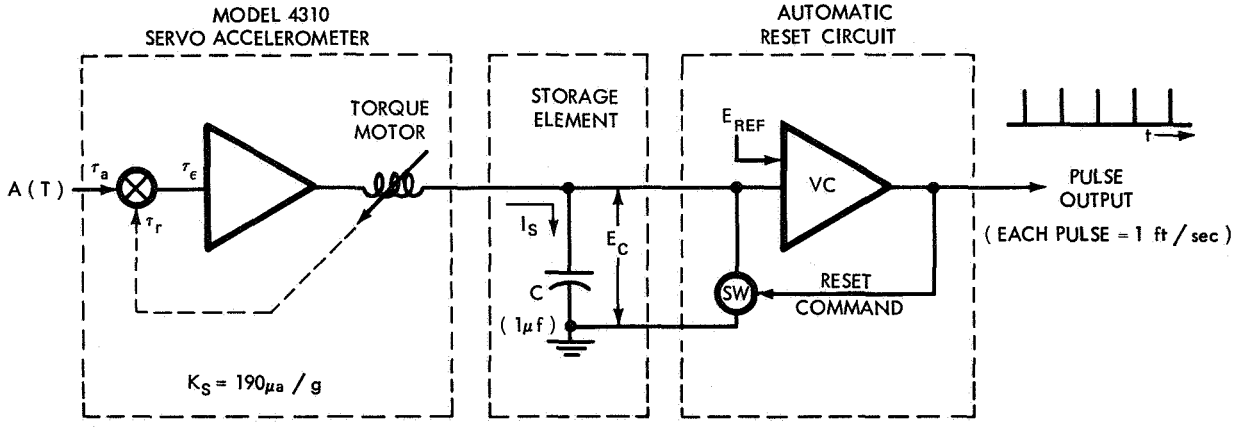

Figure 15—Simplified block diagram of Model 7300 digital accelerometer.

Pressure Transducer

The chamber pressure was measured using a pressure transducer (Bourdon tube potentiometric-type, Bourns Model 725) as an end instrument. The pressure transducer was attached to a small bracket assembly mounted and bonded with Epoxy cement on the FW-4 head near the pyrogen. A short stainless-steel tube (1/4-inch in diameter and approximately 9-inch in length)

was used to connect the pressure transducer to the chamber-pressure port of the pyrogen headcap. High-pressure stainless-steel fittings (Parker) were used to complete the assembly. Pressure checks of the system were made before flight to ensure leaktight junctions. Calibrations were made using a portable nitrogen tank supply and a standardized laboratory-type pressure gauge before final installation. Pressure range was nominally 0 to 800 psia, and calibration was found to be linear except for the region between 700 and 800 psia (See Appendix C).

Analog Longitudinal Accelerometer

The longitudinal acceleration was measured using a linear servo-type accelerometer (Kistler 303B). This sensor exhibits negligible cross-axis sensitivity, and its linearity is claimed to be better than 0.01 percent. Voltage sensitivity of one-fourth volt/g was used, resolving power being limited by other telemetry electronic components.

DISCUSSION OF ERRORS

The velocity meter, an inherently high-resolution device, is subject to several errors. Because the meter uses an analog output from a servo-type accelerometer, its minimum error is limited to the error characteristics of the sensor. Vibrations that could contribute to error are reduced by fluid damping. Integrator drift primarily is caused by sensor null errors, which are reduced by a voltage comparator tripped at exceedingly low-current levels (approximately 10^{-7} ampere). If a constant acceleration is applied, the capacitor charges linearly, but it requires a finite time to discharge or reset. For the output frequency to be directly proportional to the acceleration, the reset time should be zero. The manufacturers of the Model 7300 claim a design improvement that obviates the necessity for zero reset time. The improvement eliminates this potential error, which should show up as a nonlinearity with applied acceleration. Departure from linearity is below 20 milli-g's or 0.1 percent for a 20-g, full-scale accelerometer range.

Cross-axis sensitivity can be held to low levels by use of the proper method of suspending the seismic mass. The manufacturer claims a sensitivity of less than 2 milli-g's per g cross-axis sensitivity when 20 g's are applied to the sensitive axis.

Case-alignment error arises when the motion of the seismic mass does not parallel the reference surfaces of the case. A nominal value of case alignment to within one-fourth degree to true sensitive axis is claimed. Higher alignment accuracy can be attained at additional expense.

Spin error arises when the alignment of the true sensitive axis of the sensor does not lie parallel to the spacecraft spin axis; the magnitude of the error depends upon the degree of off-center mounting and magnitude of spin rate or centripetal acceleration.

Time delay is the time between application of an accelerating force and presence of an output pulse; 10 milliseconds is the claimed response time of the instrument.

CONCLUSIONS

Inflight performance measurements made on the FW-4D solid-propellant rocket motor used as a Delta 50 third stage showed a near-nominal thrust-time curve as constructed from the chamber pressure, longitudinal acceleration, and high-resolution velocity meter (digital accelerometer). The thrust-time curves obtained compare favorably with previous flight tests but show a slight loss in propellant specific impulse from that obtained in ground-test results. The high-resolution digital accelerometer detected a slight but continuous increase in velocity after burnout lasting for approximately 50 seconds, presumably caused by outgassing. The propellant specific impulse based upon manufacturers' stated propellant weight, with the outgassing effect neglected, was 283.3 seconds, based upon the measured effective I_{sp} of 281.2 seconds, which corresponds to a total impulse of 172,100 lb-sec. When the additional impulse during the outgassing period is included, the calculated propellant specific impulse rises to 284.1 sec, yielding a total impulse of 172,600 lb-sec. Use of a digital accelerometer for the accurate determination of incremental velocity is highly recommended for those missions where injection velocity is critical. A discussion of the errors shows that the absolute-velocity error is affected strongly by any misalignment as in off-center mounting even though the end instrument itself has a low inherent cross-axis sensitivity. While the technique applied permits a theoretical resolution of 1 ft/sec in 100,000 ft/sec, the method accuracy is probably no better than one-fourth percent in absolute values as used here. With precision mounting and without coning, accuracy could attain 0.1 percent. It has proven capable of detecting relative differences in velocity for 1-second intervals to better than 1 part in 300. This level is beyond that attainable by other conventional flight instrumentation.

Table 4 is a summary of the results of all FW-4 rocket motor tests for which data are available. The results indicate a close agreement for the last four flight tests based upon orbital reconstruction of third-stage velocity. Table 5 compares the predicted and 3-sigma values for the significant parameters required for a successful orbit and the reconstructed values produced by Douglas Aircraft Co. from orbital information with values calculated from third-stage performance instrumentation described in this report.

Table 4

Summary of FW-4 Performance.

Use of motor	S/N	Date	Location	Total prop. wt. (lb)	Total loaded wt. (lb)	S/C + 3rd stage wt. at ignition (lb)	S/C wt. (lb)	Spin rate (spin)	t_a (seconds)	I_{sp} Vac (lb-sec/lb)	Vac I_t (lb-sec)	Ref	$\int dt$ (psia-sec)
Test-static, altitude (PFRT)	20003	12/8/64	AEDC	598.9				200	31.3	284.98	170,680	Load cell	20,595
Test-static, altitude (PFRT)	20002	12/10/64	AEDC	600.6				201	31.0	284.4	170,790	LC	20,623
Test-static, altitude (PFRT)	20004	12/15/64	AEDC	598.8				0	failed after 2.3 seconds				
Test-static, altitude (PFRT)	20024	4/12/65	AEDC	603.2				0	31.5	286.4	172,722	LC	20,639
Test-static, altitude (PFRT)	20030	4/20/65	AEDC	606.6				202	29.5	286.4	173,717	LC	20,767
Test-static, altitude (PFRT)	20035	4/22/65	AEDC	610.3				201	30.8	285.6	174,316	LC	20,438
Test-static, altitude despin	30104	2/18/66	AEDC	606.5				200.7	28.6	283.8		LC	19,862
Delta 38 (AE-B)	20033	5/25/66	ETR	606.8	706.96	1192.3	485.35	97.0	30.82	283.93	172,287	Telemeter	19,580
Delta 39 (AIMP-D)	00001	7/1/66	ETR	608	739	946	207.5	139.2	32.5	284.3	172.850	Telemetered	
Delta 40 (Pioneer-B)	00002	8/17/66	ETR	606.2	712	851	138.9	111	30.82	283.6	171,896	Orbital reconst	
Delta 42 (Intelsat II, F-1)	00003	10/26/66	ETR	607.8	691	1049	357.6	115.5	30.72	284.1	172,659	Reconst	
Delta 44 (Intelsat II, F-2)	00004	1/11/67	ETR	610.3	685.1	1042.3	357.2	117.6	30.8	284.0	171,501	Reconst	
Delta 47 (Intelsat II, F-3)	00005	3/22/67	ETR	613.8	690.3	1046.6	356.3	109.5	30.8	284.1	173,089	Reconst	
Delta 49 (IMP-F)	40101	5/24/67	WTR	613.4	697.9	860.4	162.6	119.0	30.8	283.9	172,865	Reconst	
Delta 50 (AIMP-E)	00006	7/19/67	ETR	607.5	707.7	937.1	229.4	146.4	30.8	284.1	172,600	Telemetered	20,540
Scout 131	20038	8/10/65	Wallops	608.5	663.8	707.8	44.0	184.3	29.2	282.9	172,135	Telemeter	20,333

Table 5

Comparison of Predicted and Actual Significant Parameters.

Parameter	Required		Actual	
	Predicted	3σ Deviation	Orbital reconstruction	Telemetered
Effective specific impulse, lb-sec/lb	282.2	±2.0	282.1	282.0
Propellant specific impulse, lb-sec/lb	284.304	±2.1	284.2	284.1
Total impulse, lb-sec	172,772.6		172,764.6	172,600
Impulsive velocity, ft/sec	9621.118	±71	9620.66	9610

ACKNOWLEDGMENTS

The author is indebted to Norman Beck for the velocity meter concept and to Robert Conrad for the fabrication, assembly, and checkout of the instrumentation and telemetry system. Other members of the Instrumentation Branch and Delta Project helped in various aspects of the data display and reduction. Since the experimental results were acquired only at the end of a long chain of properly executed events from the assembly of the launch vehicle to the recording of the telemetered data, it is impossible to recognize individually all the people who have made this study possible. Nevertheless, the author wishes to acknowledge gratefully Richard Young and Ray Stottel who worked closely with the telemetry instrumentation for their continuous effort without which this study could not have been successfully undertaken.

Goddard Space Flight Center
National Aeronautics and Space Administration
Greenbelt, Maryland, February 29, 1968
492-11-00-05-51

REFERENCES

1. "Flight Report for Delta S/N 467/20207/20205, Delta Program Mission no. 39, Spacecraft: AIMP-D," Douglas Aircraft Company Report No. SM 52424, Sept. 1966.

2. White, D. W., and Harris, J. E., "Results of Testing UTC XSR 57-UT-1 Solid Propellant Rocket Motors Under the Combined Effects of Simulated Altitude and Rotational Spin," AEDC-TR-65-150, July 1965.

3. Stuart, T., "Performance of the FW-4 Third Stage Motor Delta 38," Goddard Space Flight Center Document X-470-67-117, February 1967.

4. Memo from R. W. Conrad to W. R. Schindler, AIMP-E/Delta Third Stage Telemeter, dated May 18, 1967.

5. "Flight Report for Delta Vehicle S/N 467/20207/20205, Delta Program Mission No. 39, Spacecraft: AIMP-D," Douglas Aircraft Company Report No. SM-52429, September 1966.

6. Miller, D. L., and Travis, E. W., "The AIMP-D Launch Operations Log," Goddard Space Flight Center Document X-723-66-472, September 1966.

7. "Flight Report for Delta Vehicle S/N 20213, Delta Mission No. 50, Spacecraft: AIMP-E," Douglas Report DAC-58706, November 1967.

8. "Delta 50, Anchored Interplanetary Monitoring Platform -E, Flash Flight Report," John F. Kennedy Space Center Report TR-561, Prepared by Delta Operations Branch, KSC-ULO, July 25, 1967.

9. "Detailed Test Objectives for Improved Delta Launch Vehicle, Spacecraft: AIMP-E," Douglas Report DAC 58554, Volume I, May 1967.

10. Madden, J. J., "Interim Flight Report, Anchored Interplanetary Monitoring Platform A-IMP Explorer XXXIII," Goddard Space Flight Center Document X-724-66-588, December 1966.

11. Dembrow, D., "Performance of X-258 Third Stage Motor, Delta 29," Goddard Space Flight Center Document X-623-65-330, July 1965.

12. Weston, H., Delta 39, "A-IMP-D Final Field Report," John F. Kennedy Space Center Report TR-523, March 8, 1967.

13. "Delta 50, Anchored Interplanetary Monitoring Platform -E (AIMP-E) Operations Summary," John F. Kennedy Space Center Report TR-55, July 17, 1967.

14. NASA News Release No. 67-178, IMP-E Launch Set July 19 at Cape Kennedy; Accession No. N 67-31436, July 8, 1967.

15. Miller, D. I., and Travis, E. W., "AIMP Retro Motor Program," Goddard Space Flight Center Document X-723-66-179, April 1966.

16. "Ballistic Nomenclature Rocket Static Tests," MIL-STD-292C, February 24, 1961.

17. "Fourth Stage Scout Rocket Motor, Development Program, Development Test Report," United Technology Center Report 2100 DTR, March 1965.

18. "Fourth Stage Scout Rocket Motor, Preliminary Flight Rating Test Report," United Technology Center Report 2100 PFRTR, June 1965.

Appendix A

Launch Preparations

-1 Day Countdown Tasks

1. Spacecraft checks
2. Third-stage ordnance installation and hookup
3. Fairing installation and ordnance hookup
4. Second-stage final preparations for fueling
5. Second-stage propellant servicing
6. First-stage fueling preparations

Launch Day Tasks

1. Spacecraft checks
2. Radio frequency interference checks
3. Final ordnance hookup (during this period, no radiation is permitted)
4. Pressurization preparation and fill
5. Tower removal
6. Final launch preparations
7. Liquid oxygen preparation and fill
8. Beacon checks
9. Terminal countdown

Appendix B

Sequence of Main Launch Events

Time	Event
0	Lift-off
42.7 seconds	Solid motors burnout
70	Solid motor separation
149.3	Main engine cutoff (MECO)
153.3	Separate second stage from 1st stage and start second-stage engine
216.2	Jettison spacecraft fairing
344	Initiate velocity control system
403.3	Turn off WECO
531.9	Second-stage engine cutoff
1315.3	End coast phase, fire spin rockets; start third-stage ignition delay squib
1316.3	Cut third-stage ignition wires
1317.3	Separate third stage from second stage and retro second stage
1330.3	Ignite third stage (FW-4)
1361.1	Burnout third stage (nominal 30.8 seconds)
1390.3	Despin
1405.3	Release paddles
1415.3	Release booms
1445.3	Separate spacecraft from third stage
1448.3	Fire tumble rockets on third stage

Appendix C

End Instruments

Bourns Pressure Transducer, Mod 725

Performance Characteristics

Pressure range (psia)	0 to 800	Overpressure effect	
Static error band	0.9%	without rupture	250% for 3 minutes
Temperature error band (-65° to 165°F)	2%	Size	1-3/4×1-3/4×1 inches
		Weight	5.5 oz
Vibration error	1.3%	Input voltage	6 vdc
Acceleration sensitivity axis AA, BB	0.05%	Output	0 to 5 vdc
axis CC	0.004%	Power rating	1-1/2 watts at 165°F
Overpressure effect		Response time	30 msec. to 65% full scale step pressure input
without calibration shift	150% for 5 minutes		

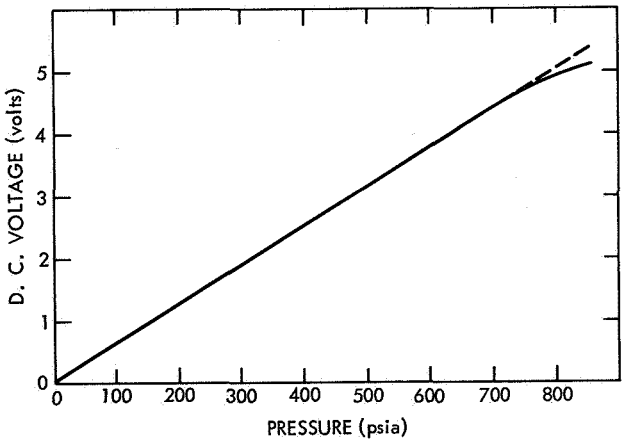

Figure C1—Performance curve Bourns pressure transducer Model No. 725, S/N 21-397.

Kistler Servo Accelerometer, Model 303B

Performance Characteristics

Acceleration range	-4g to 16g	Voltage sensitivity	125 volts/g
Output voltage	0 to 5 vdc	Linearity	0.01%

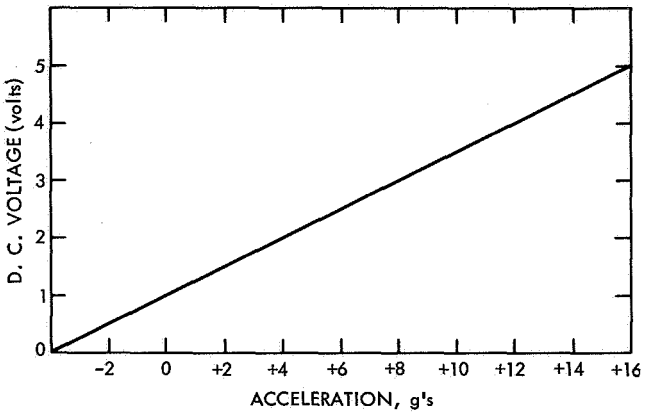

Figure C2—Performance curve, Kistler Servo Accelerometer, Model 303B.

Systron-Donner Digital Accelerometer, Model 7300

Performance Characteristics

Input voltage	28 vdc ±10%	Nominal output	20-volt amplitude pulses, 10 microseconds into 1000-ohm load
Input current	35 ma		
Vibration insensitivity	0.2 mg/g RMS maximum	Reset capability	Output pulse may be started or stopped at will
Linearity	Output pulse proportional to acceleration to 0.1%		

Appendix D

AIMP-E Spacecraft Weights

FW-4 with Spacecraft

	Weight
Propellant weight	607.5
Total weight at ignition	937.1
Spacecraft with loaded FW-4 at ignition (0.3 lb consumed)	936.8
Spacecraft with burned-out FW-4 motor	324.8
Expended weight	612.0
Inert weight consumed (estimated)	4.5

FW-Motor (S/N 00006)

	Weight
Loaded	664.3
Expended	52.3
Consumed	612.0

Weight Breakdown

	Weight	
FW-4 motor loaded	664.3	
Propellant and inert expended	612.0	
Expended FW-4	52.3	
Spacecraft AIMP-E	229.4	
Attach fitting	16.71	325.1
Third-stage TM	8.01	
Yo-yo weight, ordnance, and destruct system	13.71	
Ballast and balance	5.03	
Spacecraft with expended FW-4	324.8	

Appendix E

Summary of Measurements, Delta 50 Third-Stage Performance

Chamber Pressure

$\int_{t_0}^{t_{f_b}} P_c \, dt$ = 20,540 psia sec

$C_F A_t$ = 8.35

Ft = 171,500 lb-sec

I_{sp} = 282.1 sec

$k_1 I_{sp}$ = 280.0 sec

ΔV = 9,538 ft/sec

Accelerometer

$\int_{t_0}^{t_{f_b}} a \, dt$ = 299.34 g-sec

Ft = 172,951 lb-sec

I_{sp} = 284.7 sec

$k_1 I_{sp}$ = 282.6 sec

ΔV = 9,630 ft/sec

Velocity Meter

Ft = 172,600 lb-sec

I_{sp} = 284.1 sec

$k_1 I_{sp}$ = 282.0 sec

ΔV = 9,610 ft/sec

W_0 = 936.8 lb

W_e = 324.8 lb

$\ln \frac{W_0}{W_e}$ = 1.05919

k_1 = $\frac{607.45}{612.0}$ = 0.99256

NASA-Langley, 1969 —— 28

NATIONAL AERONAUTICS AND SPACE ADMINISTRATION
WASHINGTON, D. C. 20546

OFFICIAL BUSINESS

FIRST CLASS MAIL

POSTAGE AND FEES PAID
NATIONAL AERONAUTICS AND
SPACE ADMINISTRATION

POSTMASTER: If Undeliverable (Section 158 Postal Manual) Do Not Return

"The aeronautical and space activities of the United States shall be conducted so as to contribute . . . to the expansion of human knowledge of phenomena in the atmosphere and space. The Administration shall provide for the widest practicable and appropriate dissemination of information concerning its activities and the results thereof."

—NATIONAL AERONAUTICS AND SPACE ACT OF 1958

NASA SCIENTIFIC AND TECHNICAL PUBLICATIONS

TECHNICAL REPORTS: Scientific and technical information considered important, complete, and a lasting contribution to existing knowledge.

TECHNICAL NOTES: Information less broad in scope but nevertheless of importance as a contribution to existing knowledge.

TECHNICAL MEMORANDUMS: Information receiving limited distribution because of preliminary data, security classification, or other reasons.

CONTRACTOR REPORTS: Scientific and technical information generated under a NASA contract or grant and considered an important contribution to existing knowledge.

TECHNICAL TRANSLATIONS: Information published in a foreign language considered to merit NASA distribution in English.

SPECIAL PUBLICATIONS: Information derived from or of value to NASA activities. Publications include conference proceedings, monographs, data compilations, handbooks, sourcebooks, and special bibliographies.

TECHNOLOGY UTILIZATION PUBLICATIONS: Information on technology used by NASA that may be of particular interest in commercial and other non-aerospace applications. Publications include Tech Briefs, Technology Utilization Reports and Notes, and Technology Surveys.

Details on the availability of these publications may be obtained from:

SCIENTIFIC AND TECHNICAL INFORMATION DIVISION

NATIONAL AERONAUTICS AND SPACE ADMINISTRATION

Washington, D.C. 20546